Sources of fluids and metals and evolution models of skarn deposits in the Qimantagh metallogenic belt: A case study from the Weibao deposit, East Kunlun Mountains, northern Tibetan Plateau

Shihua Zhong[a, b, c*], Chengyou Feng[a], Reimar Seltmann[b], Alla Dolgopolova[b], Jens C. Ø. Andersen[c], Daxin Li[a], Miao Yu[d]

[a] MLR Key Laboratory of Metallogeny and Mineral Assessment, Institute of Mineral Resources, Chinese Academy of Geological Sciences, Beijing 100037, China

[b] Center for Russian and Central EurAsian Mineral Studies, Department of Earth Sciences, Natural History Museum, London SW7 5BD, UK

[c] Camborne School of Mines, University of Exeter, Penryn Campus, Tremough, Penryn, TR10 9FE, UK

[d] School of Geoscience and Environmental Engineering, Central South University, Changsha 410083, China

Abstract

The Weibao Cu-Pb-Zn deposit is typical of skarn deposits in the Qimantagh metallogenic belt (QMB), East Kunlun Mountains, northern Tibetan Plateau. It comprises three ore blocks from west to east, known as Weixi, Main and Weidong. Mineralization in the Weibao deposit is intimately related to Late Triassic intrusions occurring at Weixi and Weidong, and orebodies are predominantly hosted by the Langyashan Formaton (marine carbonate rocks), and to a lesser extent the Devonian volcanic rocks. Skarns from Weixi and Weidong are characterized by a high garnet/pyroxene ratio and diopside- and andradite-rich composition of pyroxenes and garnets, indicating a proximal, oxidized type. In contrast, skarn mineralogy of Main indicates a slightly reduced condition, typical of Pb-Zn skarn deposits. At least five hydrothermal mineralization stages can be identified and the microthermometric study indicates a general trend of cooling and dilution of the magmatic-hydrothermal fluids. Significant precipitation of Cu-Fe sulfides commenced from the fluid with the

* Corresponding author.
Email address: 809839808@qq.com (Shihua Zhong).

temperature of 340-448°C and the salinity of 2.1-15.0 wt.%. NaCl equiv. Pb-Zn sulfides however mainly precipitated when the temperatures declined to < 370°C and the salinity declined to < 7.6 wt.% NaCl equiv. Carbone, hydrogen and oxygen isotopic composition of the fluids suggests a predominantly igneous source for the initial fluids, which were modified outward by fluid-rock interaction and mixing with meteoric waters. Both sulfur and lead isotope composition of sulfides supports a mixed sulfur and metal reservoir consisting of Triassic intrusive rocks and wall rocks. Compared to early skarn-forming stages and late quartz-carbonate stages, two ore-forming stages show clear evidence of fluid boiling and fluid-rock interaction. Combined with microthermometric data of ore-forming stages, it can be deduced that fluid cooling, boiling and fluid-rock interaction were responsible for the significant metal precipitation. The Weibao deposit shows many similarities with skarn deposits in the QMB, and its genetic model therefore can be extrapolated to other skarn deposits in this region.

Key words: Fluid inclusion; stable isotope; skarn; Weibao; East Kunlun Mountains

1. Introduction:

The Weibao Cu-Pb-Zn skarn deposit is located in Xinjiang Province, NW China (latitude 37°07′58″ N, longitude 91°07′08″ E, elevation 5000 m) (Zhong et al., 2017a, b) (Fig. 1A, B), with a total ore resource of 33 million metric tons (Mt) at 0.15% Cu, 1.01% Pb, 1.22% Zn, and 9.01 g/t Ag. This deposit is one of several in the Qimantagh metallogenic belt (QMB), a significant Triassic Cu-Fe-Pb-Zn (-Ag) belt extending for ca. 550 km in East Kunlun Mountains, northern Tibetan Plateau (Fig. 1B) (Feng et al., 2010, 2012; Zhao et al., 2013). Skarn deposits in the QMB can be subdivided into several types on the basis of the dominant economic metal(s). Typical Cu-Pb-Zn skarn deposits include Kaerqueka, Hutouya, Weibao; Fe (-Cn-Zn) skarn deposits include Yemaquan, Galinge, Kendekeke; Pb-Zn skarn deposits include Sijiaoyang (Fig. 1B). These deposits were dominantly hosted by a suite of volcano-sedimentary rocks of Mesoproterozoic-Silurian age (Feng et al., 2010; Zhao et al., 2013; Zhong et al., 2017a). A range of zircon U-Pb ages of ca. 240-204 Ma for intermediate-felsic intrusions within these deposits indicate a close relationship between Triassic intrusive activity and skarn (-porphyry) mineralization (Liu et al., 2006; Wang et al., 2009; Feng et al., 2011a; Li et al., 2012, 2015; Qu et al., 2015). Published molybdenite Re-Os and muscovite $^{40}Ar/^{39}Ar$ dates within these skarn and porphyry deposits gave a similar, narrow time span ranging from 239 to 224 Ma (Li et al., 2008; Feng et al., 2009, 2011a; Gao, 2013; Tian et al., 2013; Qu et al., 2015; Yu et al., 2015), further indicating that hydrothermal events in the QMB mainly resulted from Triassic magmatic activity. Compared to geochronological work, the sources of fluids and metals of these deposits were still not sufficiently well studied. An internally consistent genetic model to explain the alteration and mineralization within these deposits has also not yet been established, which limits the understanding of the ore-forming potential in this area

and on the other hand it could serve the development of an exploration model.

In this study, we present detailed lithologic, structural, alteration, and mineralization time-space relationships of the Weibao deposit. New geochemical data presented here include the composition of skarn minerals obtained by electron microprobe analyses, fluid inclusion microthermometric and isotope analyses (oxygen, hydrogen, carbon isotopes for quartz, sulfur and lead isotopes for sulfides). The objective of this study is to (1) constrain the composition and sources of ore-forming fluids, as well as the sources of metals, (2) clarify the mechanism of alteration and metal precipitation, and (3) suggest an advanced genetic model for the Weibao deposit. By comparing with other skarn deposits in this belt, we find they show many similarities regarding the age, geological context, alteration style and especially the sources of ore-forming materials. Therefore, the genetic model proposed in this study can be extrapolated to other skarn deposits in this region.

2. Geology of the Weibao Cu-Pb-Zn deposit

At the deposit scale, the Weibao Cu-Pb-Zn deposit is composed of three ore blocks, referred to as Weixi, Main and Weidong, from west to east (Fig. 2). Stratigraphy and structural geology within three ore blocks are similar, whereas there are evident distinctions in terms of magmatic activity, alteration and mineralization. The Weibao deposit occurs at an elevation of 5000 m and surface outcrops are not well exposed. As a consequence, the geologic investigation of this study was based largely on drill cores.

2.1. Stratigraphy

Stratigraphy in the Weibao deposit includes, from oldest to youngest, the Paleoproterozoic Baishahe Formation, the Mesoproterozoic Langyashan Formation, the Middle Devonian basaltic volcanic rocks and the Triassic Elashan Formation (Fig. 2). These rocks are unconformably overlain by Cenozoic lacustrine, alluvial, and glacial sedimentary rocks.

Regionally, the Baishahe Formation generally crops out as tectonic windows in the overlying volcano-sedimentary rocks (Li, 2010). In the Weibao deposit it mainly occurs in the southeast (Fig. 2A) (Fang, 2015; Zhou et al., 2015). This unit comprises a suite of high-grade metamorphic rocks that underwent amphibolite to granulite facies metamorphism (Fang, 2015; Zhou et al., 2015; Zhong et al., 2017a). The Baishahe Formation is nonreactive and does not host mineralization in the Weibao deposit, although elsewhere in the QMB it may host significant Fe mineralization (Li, 2010; Feng et al., 2011b).

The most important ore host in the Weibao deposit is the Langyashan Formation (Fig. 2), which is also the host rock

of many skarn deposits of the QMB (e.g., Huyouya, Kaerqueka) (Feng et al., 2011a; Zhao et al., 2013). The Langyashan Formation is Mesoproterozoic and formed in a shallow marine environment (Chen, 2012; Gao, 2013). It is a thick sequence (up to 1500 m) of limestone with minor discontinuous lens or bends of intermediate-basic tuff, siltstone, and mudstone (Fang, 2015). Sedimentary bedding is locally well preserved. This formation was regionally metamorphosed to schist or quartzite, depending on the local composition. Its contact with the underlying Baishahe Formation is compositionally abrupt and disconformable (Fang, 2015; Zhou et al., 2015). The Devonian volcanic rocks (basalts and minor basaltic andesites) were found for the first time in the Weibao deposit by Zhong et al. (2017a). These lavas locally preserve amygdaloidal and/or porphyritic volcanic structures that make them noticeably different from other rock types (Zhong et al., 2017a). In the Weibao deposit, these lavas are also an important host to Cu-Fe mineralization.

The Elashan Formation unconformably overlies the Langyashan Formation, and mainly crops out in the southwestern part of the deposit (Fig. 2) (Fang, 2015; Zhou et al., 2015). It comprises purple red sandstone and the volcanic rock assemblages of crystal-lithic tuff, rhyolite and minor andesite and dacite. Similar to the Baishahe Formation in the Weibao deposit, this formation is nonreactive and does not host skarn mineralization (Zhong et al., 2017a).

2.2. Structural geology

Because of extensive post-hydrothermal cover rocks including Cenozoic sediments, faults in the Weibao deposit are largely deduced from geophysical surveying and drill intersections. Three main systems of faults, which strike northwest, northeast, and east, respectively, can be broadly distinguished (Fig. 2A) (Fang, 2015; Zhou et al., 2015; Zhong et al., 2017a). The northwest-striking fault system is interpreted to be produced before and/or during skarn mineralization (Zhou et al., 2015; Zhong et al., 2017a), therefore controlling skarn alteration and mineralization during the formation of the Weibao deposit (Fig. 3A, B). The northeast- and east-striking fault systems are generally post-skarn and post-mineralization, and are observed cutting early northwest-string faults (Fig. 2A), skarn and orebodies (Zhou et al., 2015; Zhong et al., 2017a). Apart from large-scale fault systems with noticeable displacement, small displacement faults and fractures are also widespread in the Weibao deposit. Slickensides observed from drill core intercepts and limited surface outcrops commonly indicate dip-slip and oblique-slip movement, although strike-slip movement is also locally recognized. Many of the small displacement faults and argillized fault zones are postskarn and postmineralization, but there are exceptions. Copper mineralization is found in some small displacement faults and argillized fault zones (Fig. 3C, D), indicating they were produced before and/or during skarn mineralization.

In the QMB, large-scale folds are rare. This is also the case within the Weibao deposit where drill core intercepts and surface outcrops have only documented small open folds in host rocks (Fig. 3E, F) (Hu et al., 2010; Fang, 2015; Zhou et al., 2015). The temporal relationships of these folds and the magmatic activity are unclear. Nonetheless, mineralization

and alteration in the Weibao deposit are locally observed occupying the hinge zones and limbs of the folds (Fig. 3E, F), indicating that at least these folds were produced before and/or during skarn mineralization.

2.3. Igneous rocks

The Weibao deposit is characterized by a wide range of igneous rocks similar to those observed in other skarn and porphyry deposits in the QMB (Wang et al., 2009; Gao et al., 2014a; Li et al., 2015; Qu et al., 2015). Spatially, these igneous rocks mainly crop out within two separate intrusive centers at Weixi and Weidong respectively (Fig. 2A) (Fang, 2015; Zhou et al., 2015). Both intrusive centers comprise compositionally and texturally complex dioritic to granodioritic intrusions of Late Triassic age (Zhong et al., 2017c, d). The first intrusive cluster, referred to as the Weixi intrusive center here, comprises mainly quartz diorite (Fig. 3G) and minor diorite and granodiorite. The other intrusive cluster, referred to as the Weidong intrusive center here, dominantly consists of pyroxene diorite (Fig. 3H, I), as well as minor (amphibole) diorite and (porphyritic) granodiorite. In either intrusive center, field relations of different intrusions are obscure due to tectonic activity and alteration, as well as the lack of a detailed geochronological study. The volumetrically dominant quartz diorite (Weixi) and pyroxene diorite (Weidong) contain disseminated chalcopyrite, magnetite, sphalerite and galena, and are believed to result in alteration and mineralization in the Weibao deposit (Fang 2015; Zhou et al., 2015). The other Late Triassic intrusions in the two intrusive clusters may also be related to the skarn mineralization, but their contributions to alteration and mineralization must be minor and local in view of their small volumes.

Apart from igneous rocks mentioned above, diabase and aplite dikes are also found in the Weibao deposit (Zhong et al., 2017a) but volumetrically less abundant. Diabase is observed in the whole mine area (Fig. 2B, C), ranging from several ten centimeters to several meters in width. Texturally, it is fine-grained with mafic minerals replaced by chlorite, carbonate and epidote. Aplite dikes however mainly crop out to the east of Weixi and are normally fine-grained, moderately porphyritic, up to several meters in width.

2.4. Alteration and mineralization

The alteration styles of Weixi and Weidong are similar. The dominant alteration of ore-forming quartz diorite and pyroxene diorite is potassic alteration, sericitic alteration, propylitization (chlorite-amphibole-epidote) and albitic alteration (Zhong et al., 2017c), which is similar to that within porphyry deposits (e.g., Wilson et al., 2007; Zhong et al., 2017e). Endoskarn is observed near the contact with underlying limestone and consists of an assemblage of epidote ± plagioclase ± pyroxene ± quartz. Mineralization in endoskarn is characterized by magnetite, chalcopyrite, pyrite, and minor sphalerite and galena. At the intrusion-limestone contact, the intrusion commonly contains many wall rock fragments that might have been captured during the ascending of magmas (Fig. 3I).

The alteration within the Langyashan Formation at Weixi and Weidong is closely associated with two intrusive clusters. Bleaching and recrystallization of limestone and/or marble are generally parallel to, or on, bedding laminations, similar to skarn deposits elsewhere (Maher, 2010). Irregular bleached patches or bands of carbonate minerals that cut bedding are also locally present (Fig. 3J). Disseminated chalcopyrite, bornite, and pyrite are found within both bleached and recrystallized layers in limestone. Calc-silicate marble, representing a transitional alteration between marble and skarn, is a gray to tan-white or palegreen rock, similar to recrystallized limestone but containing disseminated pyroxene, garnet and more sulfides. At Weixi and Weidong skarn consists dominantly of garnet, pyroxene, epidote, amphibole, quartz, and carbonate minerals. Garnet volumetrically dominates over pyroxene, but both are strongly replaced by epidote and amphibole (Fang, 2015; Zhong et al., 2017b, d). Mineralization in skarn is massive (Fig. 3K), banded or disseminated (Fig. 3L) (Fang, 2015; Zhong et al., 2017d), and consists dominantly of chalcopyrite (Fig. 3K, L), magnetite, and minor sphalerite and galena. Hydrothermal breccia is observed in areas near the two intrusive centers (Fig. 3M). This unit consists of matrix-supported, cobble-sized, subangular to angular fragments. The breccia matrix is generally composed of highly silicified and finely comminuted material of the same composition as the fragments. Where the breccia cuts through unmineralized rocks, the fragments are mainly composed of barren calc-silicate associations. Where the breccia cuts through mineralized rocks, massive sulfides and magnetite fragments are generally present.

Compared to Weixi and Weidong, Main is characterized by alteration and mineralization that are commonly observed in distal skarn deposits (e.g., Palinkaš et al., 2013). Mineralogically, skarn contain less garnet and more pyroxene (Feng et al., 2013). Similar to Weixi and Weidong, hydrous skarn minerals at Main, e.g., epidote, amphibole, are also observed replacing garnet and pyroxene. Mineralization is commonly banded (Fig. 3N, O), but disseminated mineralization can also be observed (Feng et al., 2013). Sulfides at Main are mainly sphalerite (Fig. 3N) and galena (Fig. 3O), typical of distal skarn deposits.

Based on detailed field investigations and observed cross-cutting relationships, Zhong et al. (2017b, d) identified five mineralization stages of skarn formation and ore deposition in the Weibao deposit (Fig. 4), which is adopted by this study. Stage I consists of anhydrous mineral facies, which are characterized by clinopyroxene-garnet ± wollastonite ± quartz; stage II is dominated by hydrous mineral phases, which are characterized by epidote-amphibole ± magnetite ± hematite ± quartz ± fluorite; stages III is a Cu-Fe-forming stage with typical mineral assemblages of chalcopyrite-pyrite-fluorite-quartz ± chlorite ± muscovite ± pyrrhotite ± magnetite ± sphalerite ± galena ± calcite; stage IV is a Pb-Zn-forming stage with typical mineral assemblages of sphalerite-galena-fluorite-quartz-calcite± chlorite ± muscovite ± chalcopyrite; stage V is the late barren stage, and consists of calcite-quartz ± muscovite ± chlorite. Veins are widespread in stages III-V, and typical vein types include quartz-chalcopyrite veins, quartz ± calcite-sphalerite-galena veins (Fig. 5A, B), and barren quartz ± calcite veins (Fig. 5C-D). Barren veins from stage V commonly cut ores (Fig. 5C), breccias (Fig. 3M), skarns or earlier veins (Fig. 5D). Veins from stages I and II are scarce, and only minor quartz-epidote veins can be locally

observed at stage II (Fig. 5E).

3. Samples and analytical methods

3.1 Sampling

A total of 22 handpicked rock samples from the Weibao deposit were examined in this study. Most of them were collected from drill core and only a few were collected from surface outcrops. Paragenetic relationships were studied in thin sections by transmitted polarized light microscopy, and in polished thick sections by reflected light microscopy. The main skarn minerals within these samples are garnet and pyroxene, which are locally replaced by epidote and amphibole. In some samples, replacement of pyroxene by garnet is also observed. Samples from Weixi and Weidong are characterized by high garnet/pyroxene ratios, whereas those from Main are characterized by much lower garnet and higher pyroxene. The veins within these samples are mainly quartz-epidote, quartz-chalcopyrite-(galena ± sphalerite), quartz-calcite-chalcopyrite, quartz-sphalerite-galena, and barren quartz-calcite veins, which are representative of veins from stages I to V in the Weibao deposit. The width of these veins varies significantly from 2 to 15 cm. A more detailed description for each sample is given in Supplementary Table 1.

3.2 Analytical methods

Analysis of the composition of skarn minerals (garnet and pyroxene) was carried out at the Electron Microprobe Laboratory of the Chinese Academy of Geological Sciences (CAGS), Beijing, China, using a JEOL-JXA8230 electron microprobe. Standard operating conditions were an accelerating voltage of 15 kV, a beam current of 10 nA, and a beam size of 5-μm diameter, with the analytical error of lower than 0.01% (Zheng et al., 2015). Natural minerals and synthetic oxides were used as standards. The raw data were converted to wt% oxides using the ZAF correction method. The end members of pyroxene and garnet were calculated using Geokit software (Lu, 2004).

Qualitative determinations of the composition of single fluid inclusions were conducted using an RM-2000 laser Raman probe at the Fluid Inclusion Laboratory, Institute of Mineral Resources, CAGS, Beijing, China. The Ar^{+} laser wavelength was 514.5 nm, the laser power was 40 mW, the diameter of the laser beam spot was 2 μm, and the spectrometer resolution was 1 cm^{-1}. Cooling and heating experiments for fluid inclusions were conducted using a Linkam THMS 600 freezing-heating unit at the same laboratory. The estimated accuracy of temperatures is ± 0.5°C for temperatures below 100°C, and ± 1.0°C for temperatures in the range of 100° to 600°C. Heating/cooling rates were restricted to < 10°C/min, and were reduced to 1 to 0.1°C/min near phase transformation. Freezing measurements were conducted before heating

measurements.

To examine the sources of fluids and metals, isotope analyses were carried out at the Stable Isotope Laboratory, Institute of Mineral Resources, CAGS, Beijing, China, using a MAT-253EM mass spectrometer for H-O isotopes and a MAT-251 mass spectrometer for C-S-Pb isotopes. Before isotope analysis, mineral grains (quartz, galena, sphalerite, pyrrhotite, chacopyrite) were carefully handpicked under a binocular microscope after samples had been crushed, cleaned. Minerals used for H and C isotope analyses were sieved to 40 to 60 mesh, whereas those for O, S and Pb isotope analyses were further crushed to < 200 mesh. In this study, oxygen isotope values were directly measured from quartz, whereas H and C isotope values were measured from water and from CO_2 hosted by fluid inclusions of quartz; S-Pb isotope data were measured from sulfides. The analytical procedure of C isotopes was similar to that described by Zhang et al. (2013), whereas those for H-O-S-Pb isotopes were similar to those described by Wang et al., (2016). The values of $\delta^{18}O$ and δD were reported relative to the Vienna standard mean ocean water (V-SMOW), and the analytical accuracy was better than ± 0.2‰ for $\delta^{18}O$, and ± 2‰ for δD values. Carbon isotope data were reported in per mil relative to the Pee Dee Belemnite (PDB), and the measurement accuracy was better than ± 0.1‰. Sulfur isotope ratios were reported as $\delta^{34}S$ relative to the Canyon Diablo Troilite (CDT) and the analytical reproducibility was ± 0.2‰. The analytical accuracy of lead isotopes was better than 0.05‰ for $^{208}Pb/^{204}Pb$, $^{207}Pb/^{204}Pb$ and $^{206}Pb/^{204}Pb$ values.

4. Mineralogy of pyroxene and garnet

4.1 Pyroxene

Pyroxenes from the Weibao deposit can be subdivided into three types based on the texture and chemical composition (Supplementary Table 2 and Figs. 5-6):

Pyroxene I (Fig. 5F-H): This type is white and light-green, and mainly observed at Weixi and Weidong. It is commonly replaced by garnet, late hydrous skarn minerals (e.g., epidote and amphibole), quartz, carbonate, and sulfides. Compositionally, it is predominantly diopsidic with extremely low if any Mn contents ($Di_{45-92}Hd_{8-53}Jo_{0-2}$) (Fig. 6), which is typical of skarn proximal to intrusions (e.g., Meinert et al., 2005; Maher, 2010). The hedenbergitic component in some pyroxenes is equal to or even slightly surpasses the diopsidic component, supposedly representing a transitional type between pyroxenes I and II (see below). In this study, these pyroxenes are artificially classified as pyroxene I because of their lighter color and especially lower MnO contents than typical pyroxene II. Pyroxene I from volcanic rocks usually displays depressed FeO and elevated Al_2O_3 and Ti_2O_3 contents, reflecting the high Al and Ti contents of the protolith.

Pyroxene II (Fig. 5I): This pyroxene is dark-green and mainly observed at Main. Similar to pyroxene I, pyroxene II was locally replaced by garnet, late hydrous skarn minerals (e.g., epidote and amphibole), quartz, carbonate, sphalerite

and galena. However, it is compositionally more hedenbergitic with elevated MnO contents ($Di_{23-43}Hd_{47-62}Jo_{9-17}$) (Fig. 6). This manganese-rich mineralogy is typical for Pb-Zn skarn deposits distal from intrusions (e.g., Lieben et al., 2000; Palinkaš et al., 2013). Pyroxene II can be locally observed at Weixi and Weidong, but normally displays lower MnO and FeO and higher MgO ($Di_{40-43}Hd_{47-51}Jo_{9}$) than that from Main ($Di_{23-28}Hd_{58-62}Jo_{10-17}$).

4.2 Garnet

The compositional data of garnet from the Weibao deposit are given in Supplementary Table 3 and in Fig. 7. There are at least three types of garnets:

Garnet I (Fig. 5G): This garnet is red and red-brown, subhedral, weakly anisotropic, and 50-200 μm (most <100 μm) in size. It is observed replacing pyroxene I or replaced by late skarn minerals (e.g., epidote, amphibole, quartz) (Fig. 5G) and sulfides. It has highly andraditic composition ($Ad_{64-97}Gr_{2\sim36}Sp_{0\sim1}$) (Fig. 7) and commonly occurs at Weixi and Weidong, whereas at Main site the garnet I is scarce. When the protolith is considered, garnet I is more commonly hosted by limestone than by volcanic rocks.

Garnet II (Fig. 5J): This garnet is pale, green or yellow-green, and either optically isotropic or weakly anisotropic; it is euhedral, and mostly 50-150 μm in size. It replaces pyroxene II or is altered by epidote, quartz, calcite, and sulfides. Compared to garnet I, it has a more grossularitic content ($Ad_{20-51}Gr_{48-80}Sp_{0\sim1}$) (Fig. 7). Garnet II at Weixi and Weidong is less abundant than that at Main. When the protolith is considered, garnet II is more commonly hosted by volcanic rocks.

Garnet III (Fig. 5K, L): In the Weibao deposit, this garnet is less common than garnets I and II. It is red, yellow and dark brown, highly anisotropic, euhedral or slightly subhedral, and > 500 μm (mostly > 1000 μm) in size. It is characterized by a pronounced zoning pattern from core to rim. However, its composition is complicated ($Ad_{24-95}Gr_{5-76}Sp_{0\sim3}$) and no consistent zoning pattern has been recognized. In some large garnets, the andraditic and grossularitic contents unexpectedly fluctuate from core to rim, with the pale tan areas more grossularitic and the darker areas more andraditic. Besides, despite the chemical zonation, garnet III from Weixi and Weidong generally displays much higher Fe contents and lower Al and Mn contents than that from Main.

5 Fluid inclusion study

5.1 Classification

Fluid inclusions are present in numerous minerals in the Weibao deposit. Four types of fluid inclusions, classified as B25, B75, B30H, B30C, were identified on the basis of phase composition at room temperature (25°C). The

classification system in this study is similar to a method proposed by Rusk et al. (2008). The letter "B" denotes "bubble", and the number indicates the average volume percent occupied by the bubble in inclusions of that type. The letter "H" refers to the presence of halite as a daughter minerals, and the letter "C" refers to the presence of two carbon dioxide phases (liquid and vapor CO_2). A detailed description of the studied inclusions was given in Supplementary Table 4. Most of these inclusions occur in groups or clusters, suggesting their primary origin. Other inclusions were avoided in this study, including those that showed evidence of necking or leaking and those distributed along secondary trails.

B25 fluid inclusions contain liquid and a vapor bubble that occupies 5-40 (mainly 20-30) vol percent of the inclusions at room temperature (Fig. 8A, B). These inclusions are typically equant, elongate, irregular, or have negative crystal shapes. This type homogenizes to liquid during heating, and is widespread from early to late mineralization stages in the Weibao deposit.

B75 fluid inclusions contain liquid and ca. 60 to 90 vol percent vapor at room temperature (Fig. 8A-C). They typically exhibit negative crystal shapes, or are rounded, elongate, irregular and equant. B75 inclusions homogenize to vapor during heating. They are common at stages I-IV, but are absent at stage V.

B30H inclusions contain liquid plus 20 to 40 vol percent vapor plus halite at room temperature (Fig. 8D, E). Rarely, B30H inclusions contain additional sylvite and unidentified mineral phases; however, in contrast to many skarn deposits (Yangla, Zhu et al., 2015; Hongniu-hongshan, Peng et al., 2016; Bismark, Baker and Lang, 2003; and others), most B30H inclusions from Weibao contain no other daughter minerals in addition to halite. Also in contrast to other skarn deposits, B30H inclusions from Weibao consistently homogenize by bubble disappearance. In this study, this type is only observed in garnet, pyroxene, epidote and minor quartz from stages I and II.

B30C inclusions comprise two carbon dioxide phases (liquid and vapor, which homogenized to liquid or vapor) and an aqueous phase at room temperature (Fig. 8 F). They have typically the shapes of negative crystals or are rounded and irregular. This type is only observed in calcite and quartz from stages IV and V. In both stages, most B30C inclusions homogenize completely after the disappearance of the CO_2 phase.

5.2 Microthermometry

Summarized microthermometric data are listed in Supplementary Table 5 and Figs. 9-10.

Stages I and II (Skarn-forming stages)

B25, B30H and B75 inclusions are observed within garnet and pyroxene from stages I and within epidote and quartz from stage II (Supplementary Table 4). In both stages, B25 inclusions are relatively less abundant compared to B30H and B75 inclusions and no coexistence between these inclusions is observed. Laser Raman spectroscopic analysis indicates that H_2O dominates both the liquid and vapor phases of these inclusions, peaking at 3265 and 3432 cm^{-1}. In some B25

and B75 inclusions, minor N_2 and CO_2 (Fig. 9A) can be observed. No microthermometric data were recorded for B75 inclusions because of the poor visibility especially during heating, the common lack of phase nucleation during freezing, and the typical difficulty of observing ice-melting and homogenization phenomena (Baker et al., 2004; Zhu et al., 2015). The homogenization temperature and salinity of other fluid inclusions do not show observable distinctions between different ore blocks (Fig. 10). B30H and B25 inclusions from stage I are characterized by homogenization temperatures of 496-560°C and 440-500°C, respectively, with salinity falling between 51.9-59.8 and 16.0-18.2 wt.% NaCl equiv, respectively. B30H and B25 inclusions from stage II display much lower homogenization temperatures and salinity than those from stage I, with homogenization temperatures ranging from 469 to 491 and 430 to 505°C, respectively, and salinity ranging from 30.1 to 42.4 and 11.5 to 17.3 wt.% NaCl equiv, respectively. All these results indicate that the fluids with high temperatures and moderate to high salinity prevailed during the skarn formation, similar to skarn deposits elsewhere (e.g., Meinert et al., 2003; Zhu et al., 2015; Peng et al., 2016).

Stages III and IV (Ore-forming stages)

These two stages are the main ore-forming stages in the Weibao deposit. Fluid inclusions were investigated in ore (sphalerite) and synore gangue minerals (quartz, carbonate, fluorite). B25 and B75 inclusions are widespread in stages III and IV, whereas B30C inclusions are rare and only found in carbonate and quartz from stage IV. Most of the B25 inclusions coexist with B75 inclusions and vice versa. In this study, only coexisting B25 and B75 inclusions (boiling inclusion assemblages) were measured (Fig. 8A, B). Laser Raman spectroscopic analyses indicate that H_2O dominates both the liquid and vapor phases of the measured inclusions (Fig. 9B), except for B30C inclusions (Fig. 9C).

Fluid inclusions from stage III at three ore blocks consistently homogenize in the temperature range between 340° and 448°C (peaking at 380-420°C) (Fig. 10). The coexisting B25 and B75 inclusions within samples generally show a much more narrow range (< 15°C) of homogenization temperatures. However, their salinity is variable, ranging from 2.1 to 15.0 wt.% NaCl equiv (peaking at ~8.4 wt.% NaCl equiv). These characteristics are typical of boiling fluid inclusion assemblages. The B25 and B75 inclusions from stage IV are characterized by temperatures of 288-398°C (peaking at 320-370°C) and salinity of 0.4-12.6 wt.% NaCl equiv (peaking at ca. 6.0 wt.% NaCl equiv). The B30C inclusions at stage IV homogenize in the temperature range between 299° to 356°C with salinity of 5.4-7.6 wt.% NaCl equiv. Similar to coexisting B25 and B75 inclusions at stage III, those within samples from stage IV also show a narrow temperature range (generally < 10°C) and variable salinity, indicating occurrence of fluid boiling at stage IV.

Stage V (late barren stage)

Barren quartz-carbonate veins from stage V are extensively developed at the three ore blocks. Only B25 and B30C inclusions are observed and the quantity of B30C inclusions increases compared to that from stage IV. Coexisting B25 and B30C inclusions have not been observed. Laser Raman spectroscopic analysis indicates that although the liquid phase is still dominated by water, most of the B25 inclusions contain minor CO_2 and/or CH_4 in the gas phase (Fig. 9D). All

these indicate that the fluid from stage V no longer belongs to a simple H_2O-NaCl system, but probably a H_2O-NaCl-CO_2 system. Homogenization temperatures decline to < 300°C (mostly < 240°C) at this stage, with salinity peaking at 3-4 wt.% NaCl equiv (Fig. 10). The low-temperature, low-salinity feature of the fluids at the late stage has been widely documented in many magmatic-hydrothermal systems (e.g., Zhu et al., 2015), probably suggesting the extensive involvement of low-temperature, low-salinity meteoric water (e.g., Zhang et al., 2013; Wang et al., 2016).

6 Stable and radiogenic isotopes

6.1 Hydrogen, oxygen and carbon isotopes

Hydrogen, oxygen and carbon isotope composition of fluids hosted by quartz is listed in Supplementary Table 6. No systematic variation is observed between the three ore blocks; however, they vary significantly between the mineralization stages. The δD, $\delta^{18}O$ and $\delta^{13}C$ values of five samples from stage III range from -106.7 to -89.1‰, 12.5 to 16.7‰ and -14.4 to -10.8‰ respectively. Only one sample (WX-2) is obtained from stage IV, which has lower $\delta^{18}O$ (5.8‰) and δD values (-106.3‰) and a higher $\delta^{13}C$ value of -9.5‰. $\delta^{18}O$ values from stage V significant decrease (-6.1 to -3.6‰) compared to that from stages III and IV, whereas $\delta^{13}C$ values show a trend to higher values (average: -8.4‰). In contrast, δD values from stage V (-110.5 to -91.6‰) show a similar range to those from stages III and IV.

6.2 Sulfur and lead isotopes

Sulfur and lead isotope ratios of sulfides separated from skarn and ores are reported in Supplementary Table 7. The sulfur isotope composition ($\delta^{34}S$) of sulfides at Weixi and Weidong ranges strictly from 1.8-4.1‰ and 2.7-3.9‰ respectively. Only one sulfide sample was collected from Main which has a $\delta^{34}S$ value of 2‰. When it comes to lead isotopes, no systematical variation is observed between and/or within sulfides, mineralization stages, or ore blocks. Measured sulfides consistently display a narrow range of $^{206}Pb/^{204}Pb$ (18.732-18.364), $^{207}Pb/^{204}Pb$ (15.587-15.709) and $^{208}Pb/^{204}Pb$ values (38.022-38.417). Since $^{238}U/^{204}Pb$ and $^{232}Th/^{204}Pb$ values of sulfides are negligible, these measured $^{206}Pb/^{204}Pb$, $^{207}Pb/^{204}Pb$ and $^{208}Pb/^{204}Pb$ values can be regarded as the initial ratios. These values of sulfur and lead isotopes are broadly consistent with those reported by Gao et al. (2014b) and Fang (2015) (Supplementary Table 7).

7. Discussion

7.1 Skarn types and redox conditions

Many studies illustrated that garnet and pyroxene composition could provide unique fingerprints to classify the skarn type (Einaudi and Burt, 1982; Nakano et al., 1994; Zaw and Singoyi, 2000; Somarin, 2004). By detailed investigations of the chemical composition of pyroxenes from 46 skarn deposits in Japan, Nakano et al. (1994) demonstrated that the Mn/Fe ratio of pyroxene in each deposit was relatively constant and tended to vary regionally in accordance with metal types. He suggested that most pyroxenes from Cu-Fe skarn deposits were characterized by a low Mn/Fe ratio (<0.1), whereas those from Pb-Zn skarn deposits had a higher Mn/Fe ratio (>0.2) (Nakano et al., 1994). Besides, according to a detailed study of 15 representative skarn deposits worldwide, Einaudi and Burt (1982) found an increase in grossular and spessartine + almandine and a decrease in andradite contents of garnets through the deposit sequence Cu→Fe→Zn-Pb→W.

At Weixi and Weidong where copper mineralization noticeably prevails, the predominant pyroxenes are diopsidic (pyroxene I) with a consistent Mn/Fe ratio strictly ranging from 0.00 to 0.04, whereas garnets are dominantly andraditic. At Main where Pb-Zn mineralization is predominant, the observed pyroxenes are generally Fe- and Mn-rich (pyroxene II) and have a distinctly elevated Mn/Fe ratio ranging from 0.17 to 0.29 (mostly >0.20). Moreover, compared to Weixi and Weidong, the aluminum-rich garnet II prevails at Main. Therefore, the composition of clinopyroxene and garnet in the Weibao deposit suggests that on the basis of the dominant economic metals, skarns at Weixi and Weidong are Cu skarns, whereas skarns at Main are Pb-Zn skarns.

Apart from classifying skarn types, skarn minerals can also be used to evaluate the oxidation state of the mineralization fluids (e.g., Zaw and Singoyi, 2000; Maher, 2010; Zhang et al., 2017). The high garnet/pyroxene ratio at Weixi and Weidong, as well as the diopside-rich and andradite-rich composition of pyroxenes and garnets, is consistent with those in Cu-(Fe-Au) skarn deposits elsewhere (Zaw and Singoyi, 2000; Maher, 2010; Zhang et al., 2017) and advocates a proximal, oxidized skarn environment at Weixi and Weidong. Garnet at Main is however less developed than pyroxene. This feature, as well as the hedenbergite-rich and grossular-rich composition of pyroxenes and garnets, is consistently indicative of a less oxidized or slightly reduced environment at Main (Zaw and Singoyi, 2000; Palinkaš et al., 2013). Since skarns at Weixi and Weidong are spatially proximal to intrusions, the nature of the high oxygen fugacity therefore might be inherited from magmatic fluids extracted from these intrusions. In contrast, the feature of relatively low oxygen fugacity of skarns at Main suggests that the magmatic fluid might be modified during its relatively long-distance infiltration through the country rocks, which is consistent with stable isotope evidence in this study (see section

7.3 for more discussions).

7.2 Pressure estimates

There is a consensus that estimates of trapping pressure can only be obtained if an independent trapping temperature is known or if fluid inclusions were trapped under immiscible or boiling conditions (Roedder and Bodnar, 1980; Baker and Lang, 2003; Seo et al., 2012). Petrographic evidence for boiling is exhibited at stages III and IV where B25 and B75 inclusions coexist. Microthermometry reveals that these coexisting B25 and B75 inclusions show similar homogenization temperatures but variable salinity, further demonstrating they were trapped under boiling conditions (Baker and Lang, 2003). In Fig. 11, a range of pressure values from 200 to 400 bars is obtained for the boiling inclusion assemblages at stage III. This range therefore can represent relatively exact estimates of their trapping pressure. Many studies demonstrated that cooling to a temperature below approximately 400°C will result in a transition from ductile to brittle rock behavior, and therefore causing a change from lithostatic to hydrostatic conditions (Fournier, 1991, 1999; Meinert et al., 2003). This means that in the Weibao deposit the brittle-to-ductile transition of the host rocks broadly occurred in the same temperature range of Cu precipitation (peaking at 380-420°C). Therefore, the varied trapping pressure (200-400 bars) for stage III would be consistent with fluctuations between lithostatic and hydrostatic pressure conditions at ~1.5 km paleodepth (a rock density of 2.7 g/cm^3). Pressure for boiling assemblages at stage IV extends to lower values, ranging from 150 to 300 bars. However, true pressure of fluids at stage IV is probably higher than that indicated by the simple NaCl-H_2O model system (Driesner and Heinrich, 2007) (which is adopted in study), because of the presence of CO_2 (Seo et al., 2012). Therefore, despite the lower trapping pressure obtained from Fig. 11, the fluid inclusions from stage IV might be trapped at a similar depth to those from stage III (~1.5 km paleodepth).

Only B25 and B30C inclusions are observed at stage V, thus precluding immiscibility. At stages I and II coexisting between different types of fluid inclusions is also not observed, resulting in uncertainty whether these inclusions were trapped under phase separation. Therefore, obtained pressure from Fig. 11 for those fluid inclusions can only represent minimum rather than true estimates of trapping pressure. Minimum trapping pressure of 300 to 600 bars is estimated for fluids from stages I and II. These values are consistent with a lithostatic condition at 1.1-2.2 km (averaging 1.65 km) paleodepth. In contrast, the fluid inclusions from stage V have much lower minimum trapping pressure of < 100 bar, consistent with a hydrostatic condition of < 1 km paleodepth. The widespread B30C inclusions at stage V also indicate that this pressure is underestimated (Seo et al., 2012).

7.3 Origin of fluids and metals

7.3.1 Hydrogen, oxygen and carbon isotope constraints

In Figs. 12 and 13, hydrogen, oxygen and carbon isotope results from this study, as well as those from Fang (2015) and Zhong et al. (2017b), are plotted to examine the sources and evolution processes of fluids in the Weibao deposit.

It can be seen that samples from stage II broadly plot into the area of "magmatic water", therefore suggesting a dominant magmatic origin of skarn-forming fluids (Fang, 2015; Zhong et al., 2017b). However, compared to typical magmatic water, fluids at stage II show a shift to higher $\delta^{18}O$ values (Supplementary Table 6; Fig. 12), probably implying that primary magmatic water had been slightly modified during its infiltration through the country rocks. This is because the country rocks within the Weibao deposit are mainly marine carbonate rocks (i.e., the Langyashan Formation), which are characterized by high $\delta^{18}O$ values (20-30 ‰) owing to the high contents of the organic material (Fang, 2015; and references therein).

Compared to stage II, stage III is characterized by much lower δD values and slightly higher $\delta^{18}O$ values of fluids (Fig. 12). The higher $\delta^{18}O$ values probably suggest much more extensive interaction of the mineralization fluids with marine carbonate rocks. The low δD values were previously explained to result from involvement of meteoric water (Fang, 2015), or from extensive magma degassing (Zhong et al., 2017b), both of which would be common during the transition from closed to open ore-forming systems. However, neither model is entirely satisfactory since an extensive involvement of meteoric water would significantly decrease the $\delta^{18}O$ values, whereas the sole magma degassing would not change the $\delta^{18}O$ values (Taylor et al., 1983; Meinert et al., 2003). Alternatively, decreased δD values could be attributed to the influence of δD-depleted organic matter in the carbonate host rocks, as suggested by other studies (Charef and Sheppard, 1987). This explanation is further supported by lower $\delta^{13}C$ values of the fluids at stage III (Fig. 13). In magmatic-hydrothermal systems, common carbon sources are inorganic carbon in seawater or marine limestone (near 0‰) (Rye and Ohmoto, 1974), organic carbon in sediments (-27 to -19‰) and juvenile carbon exsolved from magmas (-9 to -2‰) (Cocker et al., 1982; and references therein). The highly negative $\delta^{13}C$ values (-14.4 to -10.8‰) of fluids from stage III at Weixi and Weidong (Fig. 13) therefore can only be achieved with the involvement of organic matter.

The mineralization fluids from stage IV show lower $\delta^{18}O$ and higher $\delta^{13}C$ (Figs. 12 and 13) compared to stage III, although the δD values do not vary significantly (Fig. 12). The low $\delta^{18}O$ and high $\delta^{13}C$ values are consistent with a decreased contribution from fluid-rock interaction. The weakened fluid-rock interaction might be companied by increasingly enhanced involvement of meteoric water. At stage V, the fluids in the Weibao deposit are characterized by much lower $\delta^{18}O$ values and higher $\delta^{13}C$ values than those from the earlier stages. In Fig. 12, they plot into the area near the global meteoric water line (GMWL), demonstrating that the fluids at stage V might be dominated by cool, diluted

meteoric water. This is consistent with microthermometric data from stage V which suggest a low-temperature (<240°C), low-salinity (3-4 wt.% NaCl equiv) fluid.

7.3.2 Sulfur and lead isotope constraints

In Figs. 14A and 15, sulfur and lead isotope data of sulfides from this study, as well as those from Gao et al. (2014b) and Fang (2015), are plotted. It can be seen that no distinction of sulfur and lead isotopes is shown between different ore blocks. In Fig. 14A, the $\delta^{34}S$ values collectively range from -2.2 to 4.1‰. Such a sulfur isotope feature mainly points to a magmatic origin, which is common in porphyry and skarn systems worldwide (-5-+5‰; Ohmoto and Rye, 1979; Palinkaš et al., 2013; Pass et al., 2014). In $^{206}Pb/^{204}Pb$ vs. $^{207}Pb/^{204}Pb$ and $^{208}Pb/^{204}Pb$ diagrams (Fig. 15), samples from the Weibao deposit are predominantly plotted into areas constrained by the mantle growth curve, the orogene growth curve and the upper crust curve. This implies that lead in the Weibao deposit was derived from a mixture of mantle and crustal sources (Pass et al., 2014).

Nevertheless, the predominant positive $\delta^{34}S$ values in the Weibao deposit (Fig. 14A) suggest incorporation of sulfur from a more ^{34}S-enriched source than magmas. This characteristic was also recorded in many skarn deposits (e.g., Ishihara et al., 2002; Peng et al., 2016; Zhang et al., 2017), which was accounted for by mixing of sedimentary and igneous sulfur (Ripley, 1981; Pearson et al., 1988). For the Weibao deposit, this explanation may also be valid considering the extremely positive $\delta^{34}S$ values (>10‰) of the Langyashan Formation (Fig. 14A) (Fang, 2015). Sulfur of the host carbonates could be extracted and migrated into the Weibao skarn system during the emplacement of the ore-forming intrusions and the convection of the resulting magmatic-hydrothermal fluids (Ishihara et al., 2002). A mixed source between sedimentary and igneous rocks could also explain the lead isotope results. When compared with lead isotopes from the Langyashan Formation and ore-related Triassic intrusive rocks in the QMB (Fig. 15), it is clearly shown that most samples from the Weibao deposit are plotted into the overlapped area of the Triassic intrusive rocks and the Langyashan Formation. This therefore suggests that both Triassic intrusive rocks and the host carbonate rocks in the Weibao deposit probably provided Pb (and maybe other metals) during the formation of the deposit.

Noticeably, in the Weibao deposit most $\delta^{34}S$ values of the coexisting sulfides increase in the order galena ≤ chalcopyrite ≤ sphalerite within samples (Fig. 14A), indicating that these cogenetic minerals were precipitated in isotopic equilibrium (Ohmoto and Rye, 1979). For sulfides from different samples, the above order is however not always the case, and therefore suggests the existence of isotopic disequilibrium. This isotopic disequilibrium, that is common in magmatic-hydrothermal systems (Corsini et al., 1980; Shelton and Rye, 1982; Pearson et al., 1988), can be interpreted as a result of the multistage depositional process (Palinkaš et al., 2013), changes of the oxidation state (Pass et al., 2014), fluid-rock interaction (Wilson et al., 2007), or mixing between sedimentary and igneous sulfur (Pearson et al., 1988). For

the complexity of the Weibao deposit, all these models are relevant to be taken into consideration.

7.4 Mechanisms for metal precipitation

One of the major tasks in studying magmatic-hydrothermal deposits is to identify physical and chemical mechanisms that are responsible for ore precipitation. In porphyry and skarn systems, sulfide deposition may be controlled by a number of processes: (1) fluid cooling (Harris and Golding, 2002; Redmond et al., 2004; Landtwing et al., 2005); (2) phase separation (fluid immiscibility or boiling) (Klemm et al., 2007; Ni et al., 2015; Xie et al., 2005; 2006); (3) interaction with wall rocks (Hemley and Hunt, 1992; Ronacher et al., 2004; Buchholz et al., 2007); (4) fluid mixing (commonly mixing of magmatic and meteoric water) (Zaw and Singoyi, 2000; Schwinn et al., 2006; Wang et al., 2016). For a particular deposit, sulfide precipitation is generally simultaneously controlled by more than one process, although the relative importance of those processes may vary between deposits (e.g., Ronacher et al., 2004).

Previous studies demonstrated that metal solubility (Cu, Pb, Zn, Fe) decreased significantly with decline of temperatures (Hemley et al., 1992; Hemley and Hunt, 1992). In the Weibao deposit, microthermometric data reveal that temperatures of ore-forming fluids sharply decreased from > ~450°C at skarn-forming stages to ca. 380-420°C during Cu-Fe precipitation (stage III), and then further decreased to 320-370°C during Pb-Zn precipitation (stage IV) (Fig. 10). These ranges just correspond to the most favorable temperature conditions for Cu (350-425 ℃) and Pb-Zn precipitation (275-375°C) in porphyry and skarn systems (Shimizu and Iiyama, 1982; Redmond et al., 2004; Landtwing et al., 2005). Therefore, sulfide precipitation in the Weibao deposit thermal was undoubtedly controlled by thermal decline. However, the variation of the stable isotope composition is at odds with what is expected from a solely cooling magmatic fluid. If cooling was the only precipitation mechanism, then the δD, $\delta^{18}O$ and $\delta^{13}C$ values of fluids would not change (Figs. 12 and 13). The observed variation patterns of stable isotopes must therefore reflect other mechanisms.

Fluid boiling can cause fluid condensation, pH increase, and oxygen fugacity decrease, and then the precipitation of sulfides (Chen and Wang, 2011), and has been recognized as an important ore-forming mechanism for many porphyry and skarn systems (Klemm et al., 2007; Ni et al., 2015; Zhu et al., 2015; Peng et al., 2016). Boiling inclusion assemblages, which are characterized by coexisting B25 and B75 inclusions with nearly constant homogenization temperatures, are commonly observed within stages III and IV. This suggests that fluid boiling was also an important ore-forming mechanism for the Weibao deposit. Besides, as discussed before, the elevated $\delta^{18}O$ and depressed δD values, as well as extremely negative $\delta^{13}C$ values, of the mineralization fluid from stage III mainly resulted from interaction of initial magmatic water with marine carbonate rocks. Reaction with the carbonate rocks could increase the pH value of ore-forming fluids (Fang, 2015), which would result in precipitation of copper considering the negative correlation between copper and pH (Martínez and Motto, 2000). Compared to stage III, fluids from stage IV show a decrease in $\delta^{18}O$ values

and an increase in $\delta^{13}C$ values, indicating a weakened influence of fluid-rock interaction. Collectively, it can be easily deduced that fluid-rock interaction was another important mechanism in controlling Cu precipitation, and to a lesser extent, Pb-Zn precipitation, in the Weibao deposit.

As mentioned before, fluid mixing also occurred in the Weibao deposit. However, it might not be a dominant driving force for metal precipitation in view of the timing of this process. Major incursion of meteoric fluid in the Weibao deposit occurred at stage V when the advection of magmatic fluid, as well as fluid-rock interaction and fluid boiling, had largely waned. Nevertheless, the efficiency of ore precipitation could, however, have been readily aided by the operation of all of these processes in concert (Baker and Lang, 2003).

7.5 An integrated model for the genesis of the Weibao deposit

A metallogenic model for the Weibao deposit is demonstrated schematically in Fig. 16.

The alteration and mineralization are spatially and temporally related to two Late Triassic intrusive centers cropping out at Weixi and Weidong. The metasomatic zones of metric size observed in the Weibao deposit rule out a pure diffusion model that can only result in metasomatism in thin reaction zones (Palinkaš et al., 2013). The long-distance and large-scale fluid transport in the Weibao deposit must be primarily controlled by pressure and temperature gradients. Small dike or stock intrusions occurring at two intrusive centers obviously could not provide enough fluid flux and thermal mass to form the observed alteration and mineralization. Thus, the mineralizing fluids might have been derived, not only from small-scale dikes, but also from the parent magma chamber below the ore deposit (Fig. 16), which is similar to skarn deposits elsewhere (e.g., Meinert et al., 2003; Palinkaš et al., 2013).

Microthermometric data obtained from B30H and B25 inclusions from skarn-forming stages (stages I and II) indicate a high-temperature (> ~450°C), high-salinity fluid. In this situation, the rocks behaved in a ductile fashion, sealing the system from significant infiltration of meteoric waters (Fournier, 1999; Meinert et al., 2003; and references therein). A minimum formation pressure of 300 to 600 bars estimated from fluid inclusions is therefore consistent with a minimum lithostatic depth at ~1.65 km paleodepth. B30H inclusions might form by fluid immiscibility (Peng et al., 2016), which is commonly found in early potassic alteration in porphyry systems and in the early stages of skarn systems (Baker and Lang, 2003; and references therein). However, for the Weibao deposit this explanation is tentative because coexisting between B30C and other inclusions are not observed. Garnet and pyroxene from stage I indicate an anhydrous character, and were locally replaced by hydrous minerals (e.g., epidote, amphibole) from stage II. High garnet/pyroxene ratio, as well as the diopside-rich and andradite-rich composition, reflects an oxidized environment at Weixi and Weidong. In contrast, the much lower garnet/pyroxene ratio, the Fe- and Mn-rich pyroxenes with an elevated Mn/Fe ratio (mostly>0.2), and the aluminum-rich garnets collectively suggest a less oxidized condition at Main.

As the underlying vapor-saturated magma chamber continued to cool and underwent crystallization, fluid continually exsolved. The transition from convective to stagnant magma-chamber crystallization occurred, which resulted from the lack of concurrent dike intrusion and/or a sharply lower fluid flux. Therefore, the ascending fluid followed a cooling path different from that of the early stage, although their composition might be similar (Shinohara and Hedenquist, 1997; Meinert et al., 2003). Stagnant crystallization resulted in sufficient cooling so that this fluid never intersected its solvus (Shinohara and Hedenquist, 1997) and a hypersaline liquid would not form at stages III and IV. Since thermal decline to a temperature below ~ 400°C could causes a change from lithostatic to hydrostatic conditions (Fournier, 1991), the slightly scarred range of trapping pressure from 150 to 400 bars at stages III and IV would thus indicate fluctuations between lithostatic and hydrostatic pressure conditions at ~1.5 km paleodepth. This depth is consistent with that for skarn. At this depth, the fluid with salinity similar to initial magmatic water will intersect the saturated vapor-pressure curve, resulting in boiling of the ascending liquid (Meinert et al., 2003). At stage V, the Weibao hydrothermal system eventually became a totally open system where the fluid was controlled by cool, dilute meteoric water with a low temperature (<300°C) and salinity (1-5 wt.% NaCl equiv).

The stable isotope composition of fluids from stage III indicates extensive infiltration metasomatism with organic matter-bearing marine carbonate rocks. The lower $\delta^{18}O$ and higher $\delta^{13}C$ of mineralization fluids from stage IV however suggest a deceasing contribution from fluid-rock interaction. Nevertheless, precipitation of Fe-Cu and Zn-Pb sulfides might be consistently boosted by fluid cooling, fluid-rock interaction and boiling. Compared to Main, significant Pb-Zn mineralization did not occur at Weixi and Weidong either because that most sulfur had been consumed during the Cu-Fe sulfide precipitation or that the fluids were initially deficient in lead and zinc. In turn, significant Cu mineralization did not occur at Main probably because most copper were precipitated when they flowed through Weixi and Weidong which are proximal to intrusions.

Such a scenario explains a complex magmatic-hydrothermal evolution process that could have resulted in a zonation in both space and time not only of the skarn mineralogy, as described earlier, but also of the mineralization in the Weibao deposit. Nevertheless, despite this complexity we conclude that the alteration and mineralization in the Weibao deposit dominantly resulted from magmatic activity, similar to porphyry Cu deposits.

7.6 Comparison to other skarn deposits in the QMB

Skarn deposits in the QMB are characterized by Cu-Pb-Zn deposits (e.g, Weibao, Hutouya, Kaerqueka, Jinren), Fe-(Cu-Zn) deposits (e.g., Yemaquan, Galinge, Kendekeke), Pb-Zn deposits (e.g., Sijiaoyang) (Fig. 1). Similar to the Weibao deposit, Late Triassic magmatic activity was widely developed in these skarn deposits, which was interpreted to be related to skarn alteration and mineralization (Liu et al., 2006; Feng et al., 2011a; Xiao et al., 2013; Qu et al., 2015; Bai et al.,

2016). The host rocks in these deposits are commonly the Langyashan Formation and/or the Tanjianshan Group, both of which predominantly consist of carbonate rocks.

In Figs. 6 and 7, we compare the pyroxene and garnet composition of Kaerqueka, Hutouya, Yemaquan and Sijiaoyang with those from Weibao. It can be seen that similar to Weibao, garnets and pyroxenes from two Cu-Pb-Zn skarn deposits (Kaerqueka, Hutouya) are mainly characterized by andradite-rich and diopside-rich composition respectively, similar to Cu skarn deposits worldwide (Meinert et al., 2005; Maher, 2010; Zhu et al., 2015; Peng et al., 2016). Compared to typical Cu skarn deposits, distal areas in the Weibao, Kaerqueka and Hutouya however contain grossular-rich garnets and hedenbergite-rich clinopyroxenes, similar to those found at Sijiaoyang and in other distal skarn deposits elsewhere (Figs. 6 and 7) (e.g., Palinkaš et al., 2013). This feature implies that both proximal and distal alteration and mineralization were well developed in Cu-Pb-Zn skarn deposits in the QMB. The composition of pyroxenes and garnets of the Yemaquan deposit are much more complex, which is consistent with the complex alteration and mineralization zonation observed in the Yemaquan deposit. The discrepancies of the skarn mineralogy among Cu-Pb-Zn, Cu-Fe-Zn and Pb-Zn skarn deposits might reflect the different nature of ore-forming magmas (e.g., oxygen fugacity, metal concentrations).

In Figs. 14B and 15, we also compare the sulfur and lead isotope composition of sulfides from Weibao with those from other skarn deposits in the QMB. Isotope composition of three typical porphyry deposits (Lalingzaohuo, Mohexiala, Wulanwuzhuer) from this belt is also shown. It can be seen that skarn deposits, as well as porphyry deposits, in the QMB have similar sources for sulfur and metal (at least for Pb). Sulfur should be predominantly derived from magmas with minor contributions from the surrounding wall rocks (Huang et al., 2013; Lai et al., 2015), except for Mahexiala (Fig. 14B). At Mohexiala, the highly enriched $\delta^{34}S$ values indicate wall rocks might be the dominant source of sulfur. Sulfide Pb isotope composition broadly coincides with the overlapped areas of wall rocks and Triassic granitoids, indicating that similar to Weibao, both magmas and wall rocks provided metals (at least Pb) for these deposits. However, the Weibao deposit displays slightly lower $^{206}Pb/^{204}Pb$ than other deposits (Fig. 15). It is not known whether this small difference is significant, but they do not appear to be reflected by alteration and mineralization types, which overlap within error.

On a whole, it can be seen that although slight discrepancies exist between different types of skarn deposits, these skarn deposits in the QMB share many similar characteristics in terms of ages, geological contexts, alteration styles and especially sources of ore-forming materials,. Therefore, the Weibao genesis model described in this study may be also applicable to other skarn deposits in the QMB.

8. Conclusions

Weidong and Weixi, which are proximal to intrusions, show proximal skarn and mineralization, whereas Main

displays distal skarn and mineralization. At least five hydrothermal mineralization stages can be identified in these three ore blocks. The hydrous (stage I) and anhydrous (stage II) skarn stages are dominantly characterized by B30H and B25 inclusions, whereas the Cu-Fe (stage III) and Pb-Zn (stage IV) sulfide stages are dominantly characterized by B25 and B75 inclusions. In contrast, the quart-carbonate stage (stage V) is characterized by B25 and B30C inclusions. Boiling fluid inclusion assemblages are only manifested at stage III and IV. Detailed microthermometric studies show a general trend of cooling and dilution of the magmatic-hydrothermal fluids from stages I to V. Pressure estimates suggest skarn alteration and sulfide precipitation occurred at the same paleodepth of ~1.5 km. H-O-C isotope results indicate that the ore-forming components were mainly of magmatic origin, but might be modified outward by fluid-rock interaction and mixing with meteoric water. S-Pb isotope composition of sulfides suggest a mixed source for sulfur and lead (and perhaps other metals). Besides, the combining of microthermometric and isotopic results collectively advocates that thermal decline, fluid boiling, and fluid-rock interaction were responsible for the metal precipitation in the Weibao deposit. The results of this study have two important implications: (1) proximal and distal skarn can form by a single magmatic-hydrothermal system after a long distance transport of fluids; (2) the genetic model of the Weibao deposit can be used to explained alteration and mineralization within other skarn deposits in the QMB.

Acknowledgements

This study was financially supported by the Geological Survey Program (Grant 1212011085528) of the China Geological Survey; the Program of High-level Geological Talents (201309) and Youth Geological Talents (201112) of the China Geological Survey; and the IGCP–592 project sponsored by IUGS–UNESCO. SZ appreciates the cooperation with the Natural History Museum (RS, AD) and the Camborne School of Mines, University of Exeter (JA) for hosting his skarn research. This is a contribution to their research on mineralized skarn systems funded by the EU Horizon 2020 project "FAME" (grant # 641650) and the Chinese Scholarship Council (fellowship to SZ). Dr. Hongying Qu, Jiannan Liu, Hui Wang and Jianhou Zhou from the CAGS are acknowledged for their assistance during the fieldwork.

References

Bai, Y.N., Sun, F.Y., Qian, Y., Liu, H.C., Zhang, D.M., 2016. Zircon U-Pb geochronology and geochemistry of pyroxene diorite in Galinge iron-polymetallic deposit, East Kunlun. Global Geology, 17-27 (in Chinese with English abstract).

Baker, T., Lang, J.R., 2003. Reconciling fluid inclusion types, fluid processes, and fluid sources in skarns: an example from the Bismark Deposit, Mexico. Mineralium Deposita 38, 474-495.

Baker, T., Van Achterberg, E., Ryan, C.G., Lang, J.R., 2004. Composition and evolution of ore fluids in a magmatic-hydrothermal skarn deposit. Geology 32, 117-120.

Buchholz, P., Oberthür, T., Lüders, V., Wilkinson, J., 2007. Multistage Au-As-Sb mineralization and crustal-scale fluid evolution in the Kwekwe district, Midlands greenstone belt, Zimbabwe: A combined geochemical, mineralogical, stable isotope, and fluid inclusion study. Economic Geology 102, 347-378.

Charef, A., Sheppard, S.M.F., 1987. Pb-Zn mineralization associated with diapirism: Fluid inclusion and stable isotope (H, C, O) evidence for the origin and evolution of the fluids at Fedj-el-Adoum, Tunisia. Chemical Geology 61, 113-134.

Chen, Y.J., Wang, Y., 2011. Fluid inclusion study of the Tangjiaping Mo deposit, Dabie Shan, Henan Province: implications for the nature of the porphyry systems of post-collisional tectonic settings. International Geology Review 53, 635-655.

Chen, Y.X., 2012. Research on the geological characteristics and tectonic atrribute of the Mesoproterozoic to Early Paleozoic metamorphic rock, East Segment of East Kunlun Orogen. Master thesis, Chang'an University.

Clayton, R.N., O'Neil, J.R., Mayeda, T.K., 1972. Oxygen isotope exchange between quartz and water. Journal of Geophysical Research 77, 3057-3067.

Cocker, J.D., Griffin, B.J., Muehlenbachs, K., 1982. Oxygen and carbon isotope evidence for seawater-hydrothermal alteration of the Macquarie Island ophiolite. Earth and Planetary Science Letters 61, 112-122.

Corsini, F., Cortecci, G., Leone, G., Tanelli, G., 1980. Sulfur isotope study of the skarn-(Cu-Pb-Zn) sulfide deposit of Valle del Temperino, Campiglia Marittima, Tuscany, Italy. Economic Geology 75, 83-96.

Driesner, T., Heinrich, C.A., 2007. The system H_2O-NaCl. Part I: Correlation formulae for phase relations in temperature-pressure-composition space from 0 to 1000°C, 0 to 5000bar, and 0 to 1 X_{NaCl}. Geochimica et Cosmochimica Acta 71, 4880-4901.

Einaudi, M.T., Burt, D.M., 1982. Introduction; terminology, classification, and composition of skarn deposits. Economic geology 77, 745-754.

Fang, J., 2015. Ore Genesis of Weibao banded skarn lead-zinc deposit, Qimantagh area, Xinjiang, China. Master Thesis, Chinese Academy of Sciences.

Feng, C.Y., Li, D.S., Qu, W.J., Du, A.D., Wang, S., Su, B.S., Jiang, J.H., 2009. Re-Os isotopic dating of molydenite from the Suolajier skarn-type copper-molybdenum deposit of Qimantage Mountain in Qinghai province and its geological significance. Rock and mineral analysis 28, 223-227 (in Chinese with English abstract).

Feng, C.Y., Li, D.S., Wu, Z.S., Li, H.J., Zhang, Z.Y., Zhang, A.K., Shu, X.F., Su, S.S., 2010. Major types. time-space distribution and metallogeneses of polymetallic deposits in the Qimangtage metallogenic belt, Eastern Kunlun area. Northwestern Geology 43, 10-17 (in Chinese with English abstract).

Feng, C.Y., Wang, X.P., Shu, X.F., Zhang, A.K., Xiao, Y., Liu, J.N., Ma, S.C., Li, G.C., Li, D.X., 2011a. Isotopic chronology of the Hutouya skarn lead-zinc polymetallic ore district in Qimantage area of Qinghai province and its geological significance. Journal of Jilin University(Earth Science Edition) 41, 1806-1817 (in Chinese with English abstract).

Feng, C.Y., Zhao, Y.M., Li, D.X., Liu, J.N., Xiao, Y., Li, G.C., Ma, S.C., 2011b. Skarn types and mineralogical characteristics of the Fe-Cu-polymetallic Skarn deposits in the Qimantage area, western Qinghai Province. Acta Geol Sin 85, 1108-1115 (in Chinese with English abstract).

Feng, C.Y., Wang, S., Li, G.C., Ma, S.C., Li, D.S., 2012. Middle to Late Triassic granitoids in the Qimantage area, Qinghai Province, China: Chronology, geochemistry and metallogenic significances. Acta Petrologica Sinica 28, 665-678 (in Chinese with English abstract).

Feng, C.Y., Li, D.X., Zhao, Y.M., Liu, J.N., Xiao, Y., Yu, M., 2013. Polycyclic tectono-magmatic evolution and metallization in the Qimantagh area, East Kunlun Mountains. Chinese Academy of Geological Sciences.

Fournier, R.O., 1991. The transition from hydrostatic to greater than hydrostatic fluid pressure in presently active continental hydrothermal systems in crystalline rock. Geophysical Research Letters 18, 955-958.

Fournier, R.O., 1999. Hydrothermal processes related to movement of fluid from plastic into brittle rock in the magmatic-epithermal environment. Economic Geology 94, 1193-1211.

Gao, Y.B., 2013. The intermediate-acid intrusive magmatism and mineralization in Qimantag, East Kunlun Mountains. Ph.D. thesis, Chang'an University.

Gao, Y.B., Li, W.Y., Qian, B., Li, K., Li, D.S., He, S.Y., Zhang, Z.W., Zhang, J.W., 2014a. Geochronology, geochemistry and Hf isotopic compositions of the granitic rocks related with iron mineralization in Yemaquan deposit, East Kunlun, NW China. Acta Petrologica Sinica, 1647-1665 (in Chinese with English abstract).

Gao, Y.B., Li, W.Y., Qian, B., Li, K., Zhang, Z.W., Jiang, Z.X., Shen, D.L., Wang, Z.H., Ye, M.F., 2014b. Geology, fluid incluisions and S, Pb isotopic geochemistry of the Weibao Zn-Pb deposit in Qimantage, Xinjiang. Journal of Jilin University (Earth Science Edition) 44, 1153-1165 (in Chinese with English abstract).

Harris, A.C., Golding, S.D., 2002. New evidence of magmatic-fluid-related phyllic alteration: Implications for the genesis of porphyry Cu deposits. Geology 30, 335-338.

Hemley, J.J., Cygan, G.L., Fein, J.B., Robinson, G.R., d'Angelo, W.M., 1992. Hydrothermal ore-forming processes in the light of studies in rock-buffered systems; I, Iron-copper-zinc-lead sulfide solubility relations. Economic Geology 87, 1-22.

Hemley, J.J., Hunt, J.P., 1992. Hydrothermal ore-forming processes in the light of studies in rock-buffered systems; II, Some general geologic applications. Economic Geology 87, 23-43.

Hu H.W., Jing B.S., Wang S.L., Shu L., 2010. Brief analysis for geological features and ore deposit origin of Weibao

lead-zinc deposit in Ruoqiang country, Xinjiang. Northwestern Geology 43, 73-80 (in Chinese with English abstract).

Huang, M., Lai, J.Q., Ma, X.L., Cao, D.Y., 2013. Geochemical chateracteristics and genesis of Kendekeke deposit in Qinghai province, China. The Chinese Journal of Nonferrous Metals 23, 2659-2670 (in Chinese with English abstract).

Ishihara, S., Kajiwara, Y., Jin, M.S., 2002. Possible carbonate origin of ore sulfur from Geumseong Mo deposit, South Korea. Resource Geology 52, 279-282.

Klemm, L.M., Pettke, T., Heinrich, C.A., Campos, E., 2007. Hydrothermal evolution of the El Teniente deposit, Chile: porphyry Cu-Mo ore deposition from low-salinity nagmatic fluids. Economic Geology 102, 1021-1045.

Lai, J.Q., Huang, M., Song, W., Su, S.S., Wang, S.L., 2015. Geochemical characterisitcs and source of ore-forming materials of Kaerqueka copper polymetallic deposit in Qinghai province, China. Earth Science-Journal of China University of Geosciences 40, 1-16 (in Chinese with English abstract).

Landtwing, M., Pettke, T., Halter, W., Heinrich, C., Redmond, P., Einaudi, M., Kunze, K., 2005. Copper deposition during quartz dissolution by cooling magmatic-hydrothermal fluids: The Bingham porphyry. Earth and Planetary Science Letters 235, 229-243.

Lei, Y.B., Lai, J.Q., Wang, X.J., Su, S.S., Wang, S.L., Tao, S.L., 2014. Origin and evolution of ore-forming material of Hutouya polymetallic deposit. The Chinese Journal of Nonferrous Metals 24, 2117-2128 (in Chinese with English abstract).

Li, G.C., Feng, C.Y., Wang, R.J., Ma, S.C., Li, H.M., Zhou, A.S., 2012. SIMS zircon U-Pb age, petrochemistry and tectonic implications of granitoids in northeastern Baiganhu W-Sn orefield, Xinjiang. Acta Geoscientica Sinica 33, 216-226 (in Chinese with English abstract).

Li, H.P., 2010. Metallogenic geological characterisitics and metallogenic prediction of Qimantage iron and polymetallic deposit of East Kunlun Mountains. Ph.D. thesis, China University of Geosciences.

Li, K., Gao, Y., Qian, B., He, S., Liu, Y., Zhang, Z., Zhang, J., Wang, Y., 2015. Geochronology, geochemical characteristics and Hf isotopic compositions of granite in the Hutouya deposit, Qimantag, East Kunlun. Geology in China, 630-645 (in Chinese with English abstract).

Li, S.J., Sun, F.Y., Feng, C.Y., Liu, Z.Y., Zhao, J.W., Li, Y.C., Wang, S., 2008. Geochronological study on Yazigou polymetallic deposit in Eastern Kunlun, Qinhai province. Acta Geologica Sinica 82, 949-955 (in Chinese with English abstract).

Li, Y.C., Li, B., Chen, J., Zhang, Q.M., 2013. Sr-Nd-Pb isotopic characterisitcs of ore-bearing granodiorites from lalingzaohuo deposit and its geological significance. Journal Mineral Petrol 33, 110-115 (in Chinese with English abstract).

Lieben, F., Moritz, R., Fontboté, L., 2000. Mineralogy, geochemistry, and age constraints on the Zn-Pb skarn deposit of Maria Cristina, Quebrada Galena, northern Chile. Economic Geology 95, 1185-1196.

Liu, Y., Mo, X., Yu, X., Zhang, X., Xu, G., 2006. Zircon SHRIMP U-Pb dating of the Jingren granite, Yemaquan region of the east Kunlun and its geological significance. Acta Petrologica Sinica, 2457-2463 (in Chinese with English abstract).

Lu, Y.F., 2004. GeoKit-A geochemical toolkit for microsoft excel. Geochimica 33, 459-464 (in Chinese with English abstract).

Ma, S.C., Feng, C.Y., Li, G.C., Su, X.F., 2012. Sulfur and lead isotope compositions of the Hutouya copper-lead-zinc plymetallic deposit in Qinghai province and their genetic significance. Geology and Exploration 48, 321-331 (in Chinese with English abstract).

Maher, K.C., 2010. Skarn alteration and mineralization at coroccohuayco, Tintaya District, Peru. Economic Geology 105, 263-283.

Martínez, C.E., and Motto, H.L., 2000, Solubility of lead, zinc and copper added to mineral soils: Environmental Pollution 107, 153-158.

Meinert, L., Hedenquist, J., Satoh, H., Matsuhisa, Y., 2003. Formation of anhydrous and hydrous skarn in Cu-Au ore deposits by magmatic fluids. Economic Geology 98, 147-156.

Meinert, L.D., Dipple, G.M., Nicolescu, S., 2005. World skarn deposits. Economic Geology 100th Anniversary Volume, 299-336.

Nakano, T., Yoshino, T., Shimazaki, H., Shimizu, M., 1994. Pyroxene composition as an indicator in the classification of skarn deposits. Economic Geology 89, 1567-1580.

Ni, P., Wang, G.G., Yu, W., Chen, H., Jiang, L.L., Wang, B.H., Zhang, H.D., Xu, Y.F., 2015. Evidence of fluid inclusions for two stages of fluid boiling in the formation of the giant Shapinggou porphyry Mo deposit, Dabie Orogen, Central China. Ore Geology Reviews 65, 1078-1094.

Ohmoto, H., Rye, R., 1979. Isotopes of sulfur and carbon. Geochemistry of Hydrothermal Ore Deposits, 509-567.

Palinkaš, S.S., Palinkaš, L.A., Renac, C., Spangenberg, J.E., Lüders, V., Molnar, F., Maliqi, G., 2013. Metallogenic model of the Trepča Pb-Zn-Ag Skarn Deposit, Kosovo: Evidence from fluid inclusions, rare earth elements, and stable isotope data. Economic Geology 108, 135-162.

Pass, H.E., Cooke, D.R., Davidson, G., Maas, R., Dipple, G., Rees, C., Ferreira, L., Taylor, C., Deyell, C.L., 2014. Isotope Geochemistry of the Northeast Zone, Mount Polley Alkalic Cu-Au-Ag Porphyry Deposit, British Columbia: A Case for Carbonate Assimilation. Economic Geology 109, 859-890.

Pearson, M.F., Clark, K.F., Porter, E.W., Gonzalez S., O., 1988. Mineralogy, fluid characteristics, and silver distribution at Real de Angeles, Zacatecas. Economic Geology 83, 1737-1759.

Peng, H.J., Mao, J.W., Hou, L., Shu, Q.H., Zhang, C.Q., Liu, H., Zhou, Y.M., 2016. Stable Isotope and Fluid Inclusion Constraints on the Source and Evolution of Ore Fluids in the Hongniu-Hongshan Cu Skarn Deposit, Yunnan Province, China. Economic Geology 111, 1369-1396.

Qiao, B.X., Pan, T., Chen, J., Yang, Y., 2015. Sulfur isotope chateracteristics and significance of Yemaquan polymetallic deposit, East Kunlun Mountains. Science and Technology Innovation Heraid 17, 45-47 (in Chinese with English abstract).

Qu, H.Y., Feng, C.Y., Pei, R.F., He, S.Y., Li, D.X., Liu, J.N., Wang, H., Zhou, J.H., 2015. Thermochronology of Hutouya Skarn-type copper-lead-zinc polymetallic ore district in the Qimantage area, Qinghai province. Acta Geologica Sinica, 498-509 (in Chinese with English abstract).

Redmond, P.B., Einaudi, M.T., Inan, E.E., Landtwing, M.R., Heinrich, C.A., 2004. Copper deposition by fluid cooling in intrusion-centered systems: New insights from the Bingham porphyry ore deposit, Utah. Geology 32, 217-220.

Ripley, E.M., 1981. Sulfur isotopic studies of the Dunka Road Cu-Ni deposit, Duluth Complex, Minnesota. Economic Geology 76, 610-620.

Roedder, E., Bodnar, R., 1980. Geologic pressure determinations from fluid inclusion studies. Annual Review of Earth and Planetary Sciences 8, 263-301.

Ronacher, E., Richards, J., Reed, M., Bray, C., Spooner, E., Adams, P., 2004. Characteristics and evolution of the hydrothermal fluid in the North zone high-grade area, Porgera gold deposit, Papua New Guinea. Economic Geology 99, 843-867.

Rusk, B.G., Reed, M.H., Dilles, J.H., 2008. Fluid inclusion evidence for magmatic-hydrothermal fluid evolution in the porphyry copper-molybdenum deposit at Butte, Montana. Economic Geology 103, 307-334.

Rye, R.O., Ohmoto, H., 1974. Sulfur and carbon isotopes and ore genesis: a review. Economic Geology 69, 826-842.

Schwinn, G., Wagner, T., Baatartsogt, B., Markl, G., 2006. Quantification of mixing processes in ore-forming hydrothermal systems by combination of stable isotope and fluid inclusion analyses. Geochimica et Cosmochimica Acta 70, 965-982.

Seo, J.H., Guillong, M., Heinrich, C.A., 2012. Separation of Molybdenum and Copper in Porphyry Deposits: The Roles of Sulfur, Redox, and pH in Ore Mineral Deposition at Bingham Canyon. Economic Geology 107, 333-356.

Shelton, K.L., Rye, D.M., 1982. Sulfur isotopic compositions of ores from Mines Gaspe, Quebec: an example of sulfate-sulfide isotopic disequilibria in ore-forming fluids with applications to other porphyry-type deposits. Economic Geology 77, 1688-1709.

Shimizu, M., Iiyama, J.T., 1982. Zinc-lead skarn deposits of the Nakatatsu mine, central Japan. Economic Geology 77, 1000-1012.

Shinohara, H., Hedenquist, J.W., 1997. Constraints on Magma Degassing beneath the Far Southeast Porphyry Cu-Au

Deposit, Philippines. Journal of Petrology 38, 1741-1752.

Somarin, A.K., 2004. Garnet composition as an indicator of Cu mineralization: evidence from skarn deposits of NW Iran. Journal of Geochemical exploration 81, 47-57.

Sterner, S.M., Hall, D.L., Bodnar, R.J., 1988. Synthetic fluid inclusions. V. Solubility relations in the system NaCl-KCl-H_2O under vapor-saturated conditions. Geochimica et Cosmochimica Acta 52, 989-1005.

Tao, S.L., Lai, J.Q., Huang, M., 2016. S and Pb isotope characteristics of Kandekeke polymetallic deposit in Qimantage region, Qinghai province and the genetic significance. Contributions to Mineralogy and Petrology 31, 182-189 (in Chinese with English abstract).

Taylor, B.E., Eichelberger, J.C., Westrich, H.R., 1983. Hydrogen isotopic evidence of rhyolitic magma degassing during shallow intrusion and eruption. Nature 306, 541-545.

Tian, C.s., Feng, C.y., Li, H.j., Cao, D.z., 2013. ^{40}Ar- ^{39}Ar geochronology of Tawenchahan Fe-polymetallic deposit in Qimantag Mountain of Qinghai Province and its geological implications. Mineral Deposits, 169-176 (in Chinese with English abstract).

Wang, S., Feng, C.Y., Li, S.J., Jiang, J.H., Li, D.S., Su, B.S., 2009. Zircon SHRIMP U-Pb dating of granodiorite in the Kaerqueka polymetallic ore deposit, Qimantage Mountain, Qinghai Province, and its geological implications. Geology in China 36, 74-84 (in Chinese with English abstract).

Wang, Y.H., Zhang, F.F., Liu, J.J., Que, C.Y., 2016. Genesis of the Fuxing porphyry Cu deposit in Eastern Tianshan, China: Evidence from fluid inclusions and C-H-O-S-Pb isotope systematics. Ore Geology Reviews 79, 46-61.

Wilson, A.J., Cooke, D.R., Harper, B.J., Deyell, C.L., 2007. Sulfur isotopic zonation in the Cadia district, southeastern Australia: exploration significance and implications for the genesis of alkalic porphyry gold-copper deposits. Mineralium Deposita 42, 465-487.

Xiao, Y., Feng, C.Y., Liu, J.N., Yu, M., Zhou, J.H., Li, D.X., Zhao, Y.M., 2013. LA-MC-ICP-MS zircon U-Pb dating and sulfur isotope characteristics of Kendekeke Fe-polymetallic deposit,Qinghai Province. Mineral Deposits 32, 177-186 (in Chinese with English abstract).

Xie, Y.L., Hou, Z.Q., Xu, J.H., Yang Z.M., Xu W.Y., He J.P., 2005. Evolution of multi-stage ore-forming fluid and mineralization：Evidence from fluid inclusions in yulong copper deposit，East Tibet. Acta Petrologica Sinica 21, 1409-1415 (in Chinese with English abstract).

Xie, Y.L., Yi, L.S., Xu, J.H., Li, G.M., Yang, Z.M., Yi S.P., 2006. Characteristics of ore-forming fluids and their evolution for chongjiang copper deposit in gangdise porphyry copper belt，Tibet：Evidence from fluid inclusions. Acta petrologica sinica 22, 1023-1030 (in Chinese with English abstract)

Xu, Q.L., 2014. Study on metallogenesis of porphyry deposits in eastern Kunlun orogenic belt, Qinghai province. Ph.D.

thesis, Jilin University.

Yu, H.Q., Zhang, D.Q., Jing, X.Y., Guan, J., Zhu, H.P., Feng, C.Y., Li, D.X., 2007. Geological characterisitics and genesis of the Ulan Uzhur porphyry copper deposit in Qinghai. Geology in China 34, 306-314 (in Chinese with English abstract).

Yu, M., Feng, C., Liu, H., Li, D., Zhao, Y., Li, D., Liu, J., Wang, H., Zhang, M., 2015. ^{40}Ar-^{39}Ar geochronology of the Galinge large skarn iron deposit in Qinghai province and geological significance. Acta Geologica Sinica, 510-521 (in Chinese with English abstract).

Zartman, R.E., Doe, B.R., 1981. Plumbotectonics—the model. Tectonophysics 75, 135-162.

Zaw, K., Singoyi, B., 2000. Formation of magnetite-scheelite skarn mineralization at Kara, northwestern Tasmania: Evidence from mineral chemistry and stable isotopes. Economic Geology 95, 1215-1230.

Zhan, X.D., 2016. Study on the metallogenic geological characterisitics and genesis of the deposit in the Middle Reach of Lalingzaohuo copper molybdenum polymetallic metallogenic in East Kunlun. Master thesis, Chang'an University.

Zhang, J., Chen, Y.J., Pirajno, F., Deng, J., Chen, H.Y., Wang, C.M., 2013. Geology, C-H-O-S-Pb isotope systematics and geochronology of the Yindongpo gold deposit, Tongbai Mountains, central China: Implication for ore genesis. Ore Geology Reviews 53, 343-356.

Zhang, Y., Shao, Y.J., Wu, C.D., Chen, H.Y., 2017. LA-ICP-MS trace element geochemistry of garnets: Constraints on hydrothermal fluid evolution and genesis of the Xinqiao Cu-S-Fe-Au deposit, eastern China. Ore Geology Reviews 86, 426-439.

Zhao, Y.M., Feng, C.Y., Li, D.X., Liu, J.N., Xiao, Y., Yu, M., Ma, S.C., 2013. Metallogenic setting and mineralization-alteration characteristics of major skarn Fe-polymetallic deposits in Qimantag area, western Qinghai Province. Mineral Deposits 32, 1-19 (in Chinese with English abstract).

Zheng, Y.F., 1993. Calculation of oxygen isotope fractionation in hydroxyl-bearing silicates. Earth and Planetary Science Letters 120, 247-263.

Zheng, W., Mao, J.W., Pirajno, F., Zhao, H.J., Zhao, C.S., Mao, Z.H., Wang, Y.J., 2015. Geochronology and geochemistry of the Shilu Cu-Mo deposit in the Yunkai area, Guangdong Province, South China and its implication. Ore Geology Reviews 67, 382-398.

Zhong, S.H., Feng, C., Seltmann, R., Li, D., 2017a. Middle Devonian volcanic rocks in the Weibao Cu-Pb-Zn deposit, East Kunlun Mountains, NW China: Zircon chronology and tectonic implications. Ore Geology Reviews 84, 309-327.

Zhong, S.H., Feng, C.Y., Ren, Y.Q., Li, D.X., Zhao, Y.M., 2017b. Characteristics and sources of ore-forming fluid from Weixi ore block of Weibao skarn Cu-Pb-Zn deposit, Xinjiang. Mineral Deposits 36, 483-500 (in Chinese with

English abstract).

Zhong, S.H., Feng, C.Y., Seltmann, R., Li, D.X., 2017c. Geochemical contrasts between Late Triassic ore-bearing and barren intrusions in the Weibao Cu-Pb-Zn deposit, East Kunlun Mountains, NW China: constraints from accessory minerals (zircon and apatite). Mineralum Deposita.

Zhong, S.H., Feng, C.Y., Li, D.X., Zhao, Y.M., Ren, Y.Q., Zhou, J.H., Liu, J.N., Wang, H., Yu, M., 2017d. Mineralogical characterisitcs of the Weixi ore block in the Weibao skarn-type copper-lead-zinc deposit, Xinjiang. Mineral Deposits 5, 1066-1082 (in Chinese with English abstract).

Zhong, S.H., Seltmann, R., Shen, P., 2017e. Two different types of granitoids in the Suyunhe large porphyry Mo deposit, NW China and their genetic relationships with molybdenum mineralization. Ore Geology Reviews 88, 116-139.

Zhou, J.H., Feng, C.Y., Shen, D.L., Li, D.X., Wang, H., Zhang, M.Y., Ma, S.C., 2015. Geochronology, geochemistry and tectonic implications of granodiorite in the northwest of Weibao deposit, Xinjiang Qimantage. Acta Geologica Sinica 89, 473-486 (in Chinese with English abstract).

Zhu, J.J., Hu, R.Z., Richards, J.P., Bi, X.W., Zhong, H., 2015. Genesis and Magmatic-Hydrothermal Evolution of the Yangla Skarn Cu Deposit, Southwest China. Economic Geology 110, 631-652.

Fig. 1. A. Simplified geological map of the northern Tibetan Plateau (modified after Zhong et al., 2017a). B. Geological map of the North Qimantagh magmatic arc showing the locations of main skarn and porphyry deposits (modified after Fang, 2015 and Feng et al., 2011).

Fig. 2. A. Simplified geological map of the Weibao Cu–Pb–Zn deposit showing the outlines of the three ore blocks and the locations of (B) and (C). B. Geological map of Weidong. C. Geological map of Weixi and Main. All these figures are modified after Zhong et al. (2017a) and references therein.

Fig. 3. Typical photographs of field occurrences and hand specimens in the Weibao deposit. A. Northwest-striking fault, Weidong, with the fracture surface filled with lensoid galena orebody. B Close-up view of lensoid galena orebody in (A). C. Argillized fault zone with bands of malachite, Weixi. D. Close-up view of the argillized fault zone in (C). E. Small open fold with malachite occupying the hinge zone, Weixi. F. Small open fold with bands of galena and sphalerite occupying the hinge zones and limbs. G. Fresh quartz diorite, Weixi. H. Fresh pyroxene diorite, Weidong. I. Dark pyroxene diorite located at the intrusion-limestone contact, Weidong, which contains skarn fragments. J. Sample showing replacement of pyroxene by massive garnet and also a vein-related irregular patch of bleaching and recrystallization. K. Massive chalcopyrite ore. L. Disseminated chalcopyrite and small patches of bleaching in the Devonian volcanic rock. M. Hydrothermal breccia cut by a barren quartz veinlet from stage V, Weixi. The breccia consists of carbonate fragments and matrix of magnetite. N. Banded Zn-dominant ore. O. Banded Pb-dominant ore.

Fig. 4. Schematic diagram showing paragenetic relationships of skarn and ore assemblages of the Weibao skarn deposit (modified after Zhong et al. 2017b, d). The widths of lines indicate relative abundances of minerals.

Fig. 5. Typical photographs showing veins and paragenetic skarn minerals in the Weibao deposit. A. Quartz-sphalerite-galena vein from stage IV, Main. B. Calcite-sphalerite-galena vein from stage IV, Weidong. C. Chalcocite-pyrite ore cut by a barren quartz-calcite vein from stage V, Weixi. D. Early stage barren quartz veinlet cut by a barren carbonate vein from stage V, Main. E. Quartz-epidote vein from stage II, Weidong. F. Aggregate of pyroxene I, Weixi (transmitted light). G. Euhedral garnet I replacing pyroxene I, but replaced by K-feldspar and epidote, Weixi (transmitted light). H. Pyroxene I vein cutting an earlier pyroxene I vein, Weidong (cross polarized light). I. Pyroxene II locally replaced by galena, Main (transmitted light). G. Subhedral garnet II coexisting with quartz and calcite, Main (transmitted light). K. Euhedral garnet III with a pronounced zoning pattern, Weixi (back-scattered electron image). L. Garnet III coexisting with sphalerite and cut by late quartz veinlet, Main (back-scattered electron image).

Fig. 6. Ternary plots showing the johannsenite (Jo) -diopside (Di) -hedenbergite (Hd) components of pyroxenes from the Weibao deposit and other skarn deposits in the QMB. Date sources: Weibao, this study; Kaerqueka, Hutouya, Yemaquan, Feng et al. (2013); Sijiaoyang, Feng et al. (2011). Weibao, Kaerqueka, Hutouya are typical of Cu-Pb-Zn skarn deposits in the QMB, whereas Yemaquan and Sijiaoyang are Fe-Cu-Zn and Pb-Zn skarn deposits, respectively. The areas for global Cu, Fe and Pb-Zn skarn deposits are from Meinert et al. (2005).

Fig. 7. Ternary plots showing the end member compositions of garnets from the Weibao deposit and other skarn deposits in the QMB. End members: Ad = andradite, Gr = grossular, Sp = almandine, Al = almandine. Data sources are as same as those in Fig. 6. The areas for global Cu, Fe and Pb-Zn skarn deposits are from Meinert et al. (2005).

Fig. 8. Typical photographs of fluid inclusions from different mineralization stages. A. Coexisting B25 and B75 inclusions in quartz from stage III. B. Coexisting B25 and B75 inclusions in sphalerite from stage IV. C. B75 inclusions in quartz from stage III. D. B30H inclusions in garnet from stage I. E. B30H inclusions in quartz from stage II. F. B30C inclusions in calcite from stage V.

Fig. 9. Raman spectra of fluid inclusions in the Weibao deposit. A. B25 inclusions from stage II with the vapor phase predominantly occupied by H_2O and minor CO_2. B. B75 inclusions from stage III with the vapor phase occupied by H_2O. C. B30C inclusions from stage IV with the vapor phase occupied by CO_2. D. B25 inclusions from stage V with the vapor phase occupied by H_2O, and minor CO_2 and CH_4. These inclusions are hosted by quartz (Qz).

Fig. 10. Homogenization temperatures and salinity histograms of fluid inclusions in the Weibao deposit.

Fig. 11. Plots of measured homogenization temperatures (°C) vs. salinities (wt.% NaCl equiv) in fluid inclusions of the Weibao deposit. Contours of pressure (bar) were calculated based on the H_2O-NaCl systems (Driesner and Heinrich, 2007). The halite saturation curve are drawn using the formula given by Sterner et al. (1988). Fluid inclusions from stages III and IV meet the criteria of those derived from boiling, and therefore the calculated pressure can represent true trapping pressure. The estimated pressure of fluid inclusions from stages I, II and V can only provide minimum trapping pressure because of the lack of direct evidence of phase separation during their formation (see text for more discussion).

Fig. 12. $\delta^{18}O$-δD diagram based on measured δD of fluid inclusions and calculated $\delta^{18}O_{fluid}$ of quartz in the Weibao deposit (modified after Taylor, 1974 and Buchholz et al. 2007). Data are from this study, Fang (2015) and Zhong et al. (2017b).

Fig. 13. $\delta^{13}C$ -$\delta^{18}O$ diagram based on measured $\delta^{13}C$ values of CO_2 in fluid inclusions and calculated $\delta^{18}O_{fluid}$ of quartz in the Weibao deposit (modified after Wang et al., 2016, and references therein).

Fig. 14. Variations of $\delta^{34}S$ values of sulfides from the Weibao deposit (A) and other skarn and porphyry deposits in the QMB (B). Data sources: Weibao, this study, Gao et al. (2014) and Fang (2015); Hutouya, Ma et al. (2012), Gao (2013) and Lei et al. (2014); Kaerqueka, Lai et al. (2015); Kendekeke, Tao et al. (2016) and Xiao et al. (2013) ; Lalingzaohuo, Zhan (2016); Mohexiala, Xu (2014); Wulanwuzhuer, Yu et al. (2007); Yemaquan, Qiao et al. (2015); Wall rocks (the Langyashan Formation), Fang (2015). Note that sulfides from same samples are connected with lines in (A). Positive slopes indicate the connected samples are in sulfur isotopic equilibrium, whereas negative slopes indicate the isotopic disequilibrium (see text for more discussions).

Fig. 15. Variations of lead isotope compositions of sulfides from the Weibao deposit and other skarn and porphyry deposits in the QMB. Growth curves are from Zartman and Doe (1981). Data sources: Weibao, this study, Gao et al. (2014b) and Fang (2015); Hutouya, Ma et al. (2012), Gao (2013) and Lei et al. (2014); Kaerqueka, Lai et al. (2015); Kendekeke, Tao et al. (2016) and Huang et al. (2013) ; Lalingzaohuo, Zhan (2016); Mohexiala, Xu (2014); Wall rocks (the Langyashan Formation), Fang (2015); Triassic granitoids, Feng et al. (2012) and Li et al. (2013).

Fig. 16. Schematic diagram showing the genesis of the Weibao deposit.

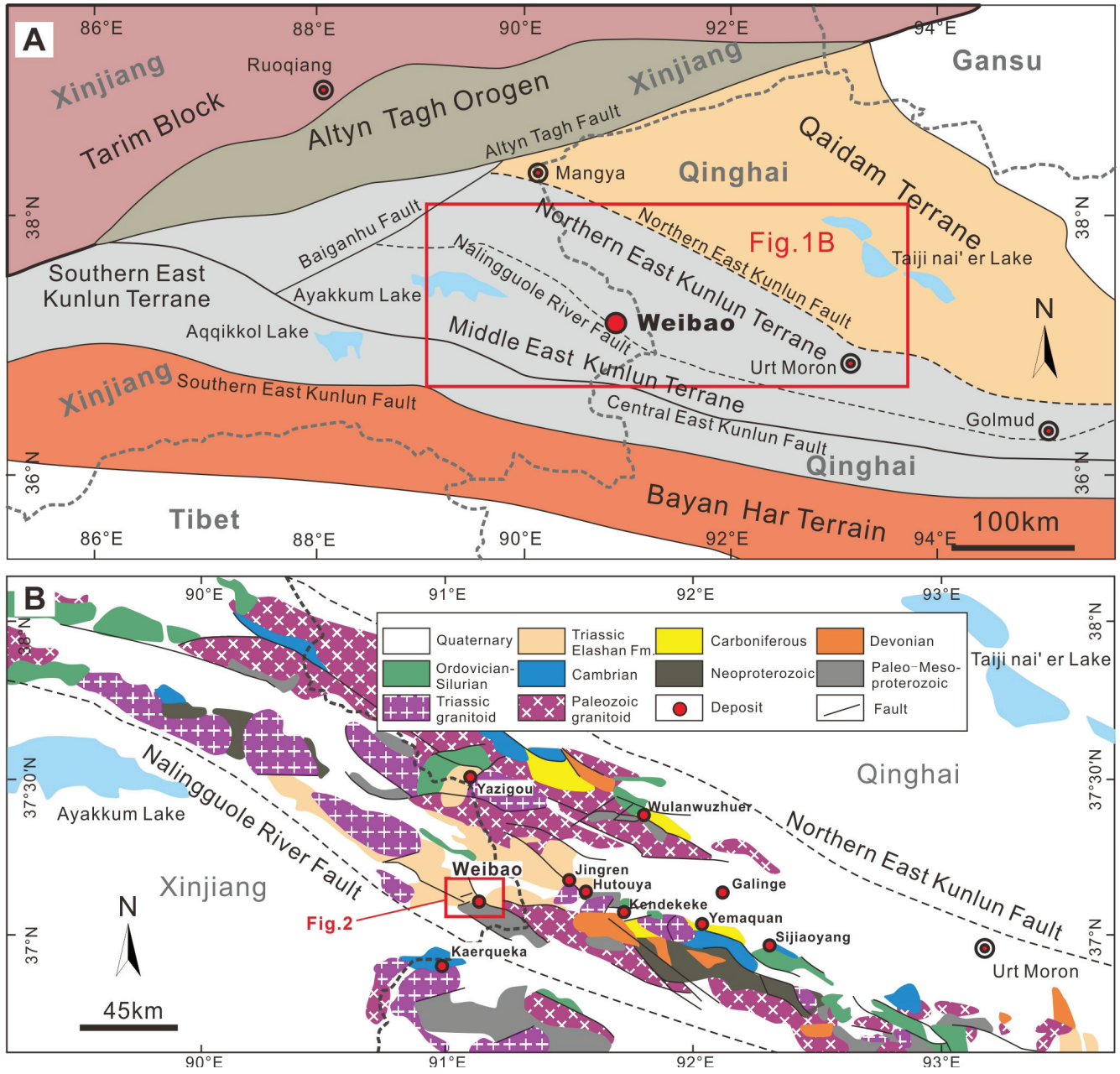
A
86°E
88°E
90°E
92°E
94°E
Xinjiang
Tarim Block
Ruoqiang
Altyn Tagh Orogen
Xinjiang
Altyn Tagh Fault
Gansu
Qaidam Terrane
Mangya
Qinghai
38°N
Baiganhu Fault
Northern East Kunlun Fault
Fig.1B
Taiji nai' er Lake
Southern East
Kunlun Terrane
Nalingguole River Fault
Ayakkum Lake
Weibao
Northern East Kunlun Terrane
N
Aqqikkol Lake
Middle East Kunlun Terrane
Urt Moron
Xinjiang
Southern East Kunlun Fault
Central East Kunlun Fault
Golmud
Qinghai
36°N
Bayan Har Terrain
Tibet
100km
B
90°E
91°E
92°E
93°E
38°N
Quaternary
Triassic Elashan Fm.
Carboniferous
Devonian
Ordovician-Silurian
Cambrian
Neoproterozoic
Paleo-Meso-proterozoic
Triassic granitoid
Paleozoic granitoid
Deposit
Fault
Taiji nai' er Lake
Qinghai
37°30'N
Yazigou
Wulanwuzhuer
Ayakkum Lake
Nalingguole River Fault
Northern East Kunlun Fault
Weibao
Jingren
Hutouya
Galinge
Xinjiang
N
Kendekeke
Yemaquan
Fig.2
Sijiaoyang
37°N
Kaerqueka
Urt Moron
45km

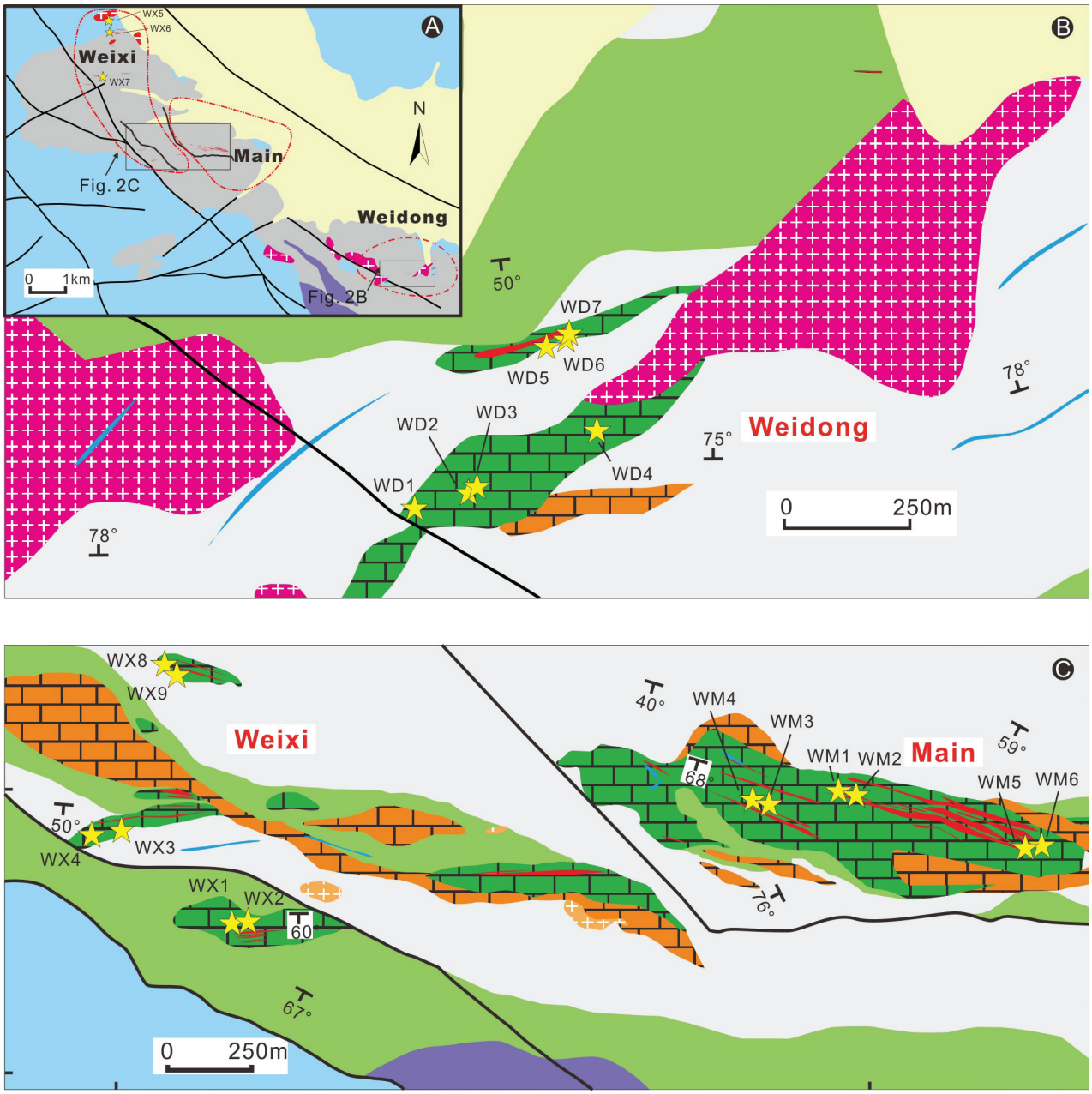

Quaternary

- Valley-fill deposits

Triassic

- Elashan Fm.
- Pyroxene diorite
- Quartz diorite
- Aplite dike
- Diabase

Mesoproterozoic

Langyashan Fm.

- Langyashan Fm.
- Limestone-dominated members
- Marble-dominated members
- Schist-dominated members

Paleoproterozoic

- Baishahe Fm.
- Skarn

- Orebody
- Fault
- 78° Strike/dip
- WX1 Sampling location and number

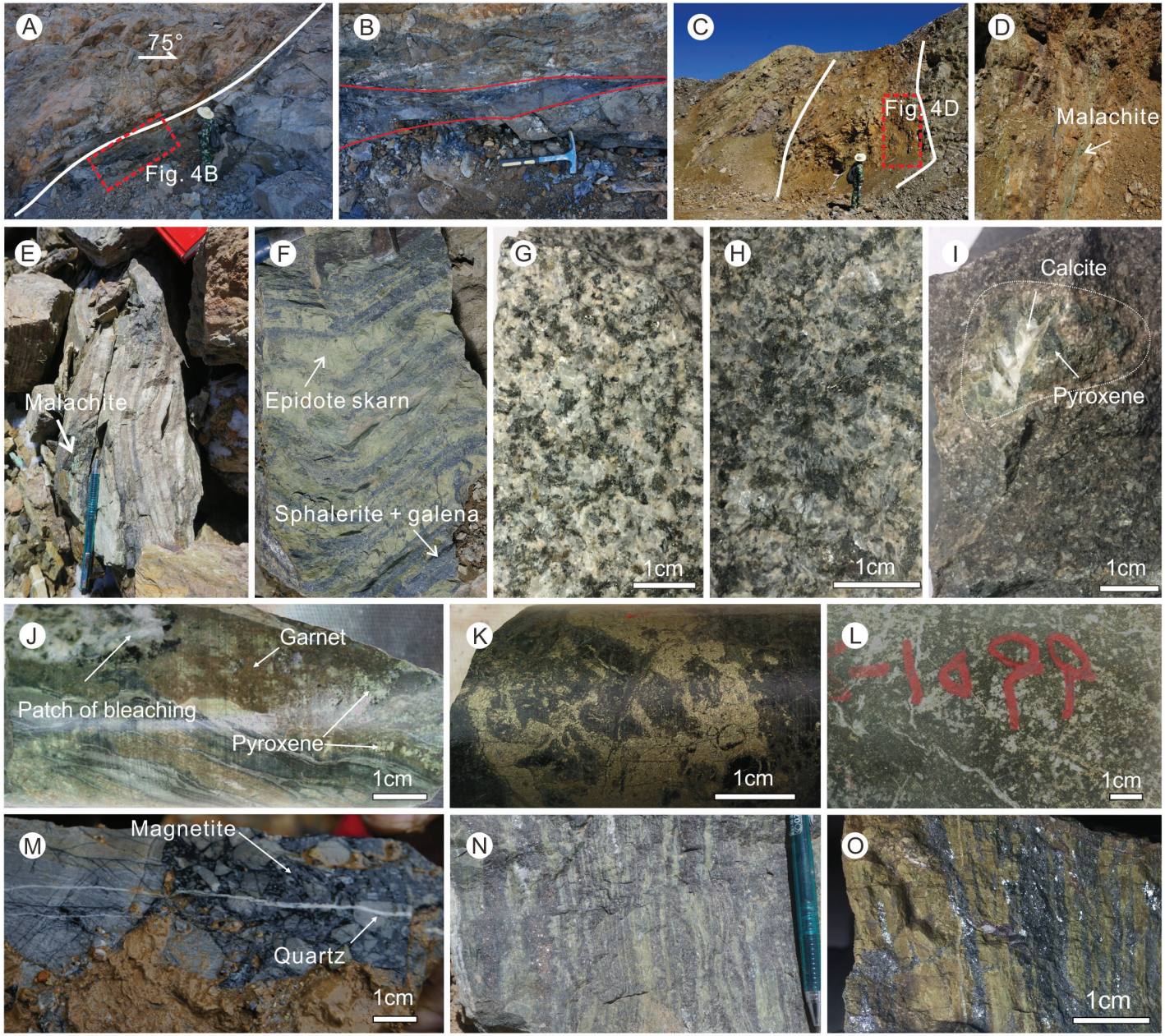
A
75°
Fig. 4B
B
C
Fig. 4D
D
Malachite
E
Malachite
F
Epidote skarn
Sphalerite + galena
G
1cm
H
1cm
I
Calcite
Pyroxene
1cm
J
Garnet
Patch of bleaching
Pyroxene
1cm
K
1cm
L
1cm
M
Magnetite
Quartz
1cm
N
O
1cm

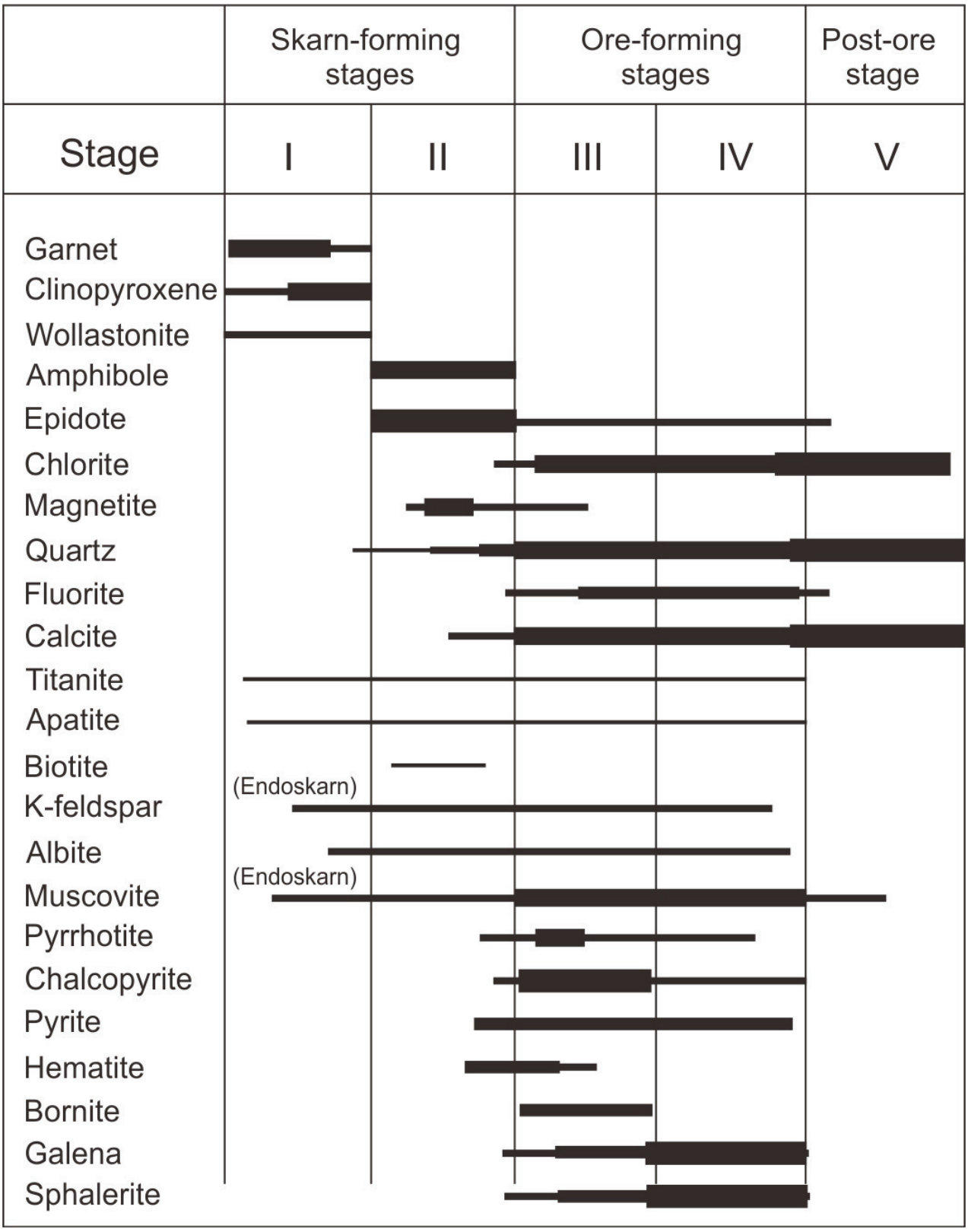
Skarn-forming stages
Ore-forming stages
Post-ore stage
Stage
I
II
III
IV
V
Garnet
Clinopyroxene
Wollastonite
Amphibole
Epidote
Chlorite
Magnetite
Quartz
Fluorite
Calcite
Titanite
Apatite
Biotite
(Endoskarn)
K-feldspar
Albite
(Endoskarn)
Muscovite
Pyrrhotite
Chalcopyrite
Pyrite
Hematite
Bornite
Galena
Sphalerite

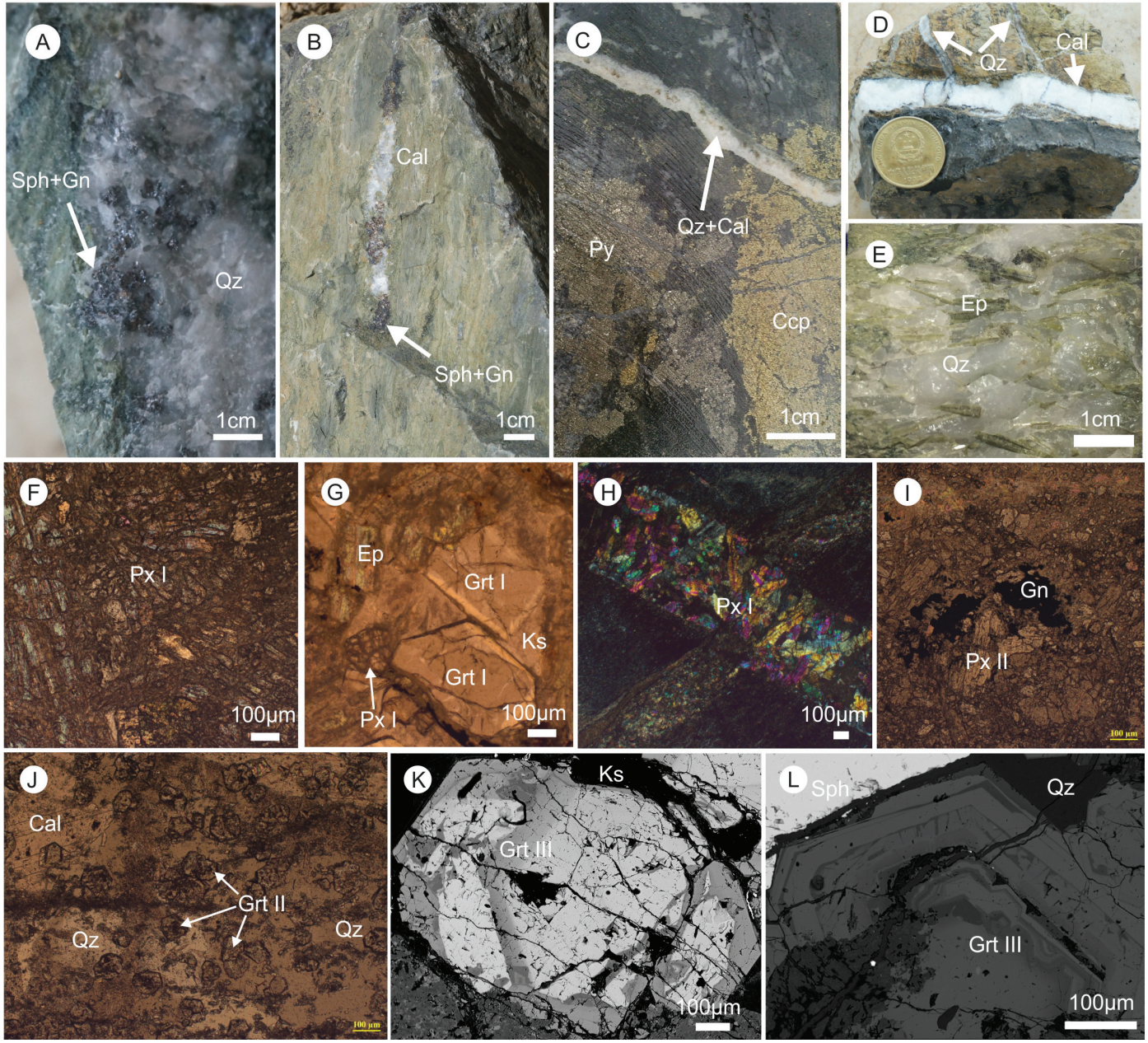
A
Sph+Gn
Qz
1cm
B
Cal
Sph+Gn
1cm
C
Qz+Cal
Py
Ccp
1cm
D
Qz
Cal
E
Ep
Qz
1cm
F
Px I
100μm
G
Ep
Grt I
Ks
Grt I
Px I
100μm
H
Px I
100μm
I
Gn
Px II
J
Cal
Grt II
Qz
Qz
K
Ks
Grt III
100μm
L
Sph
Qz
Grt III
100μm

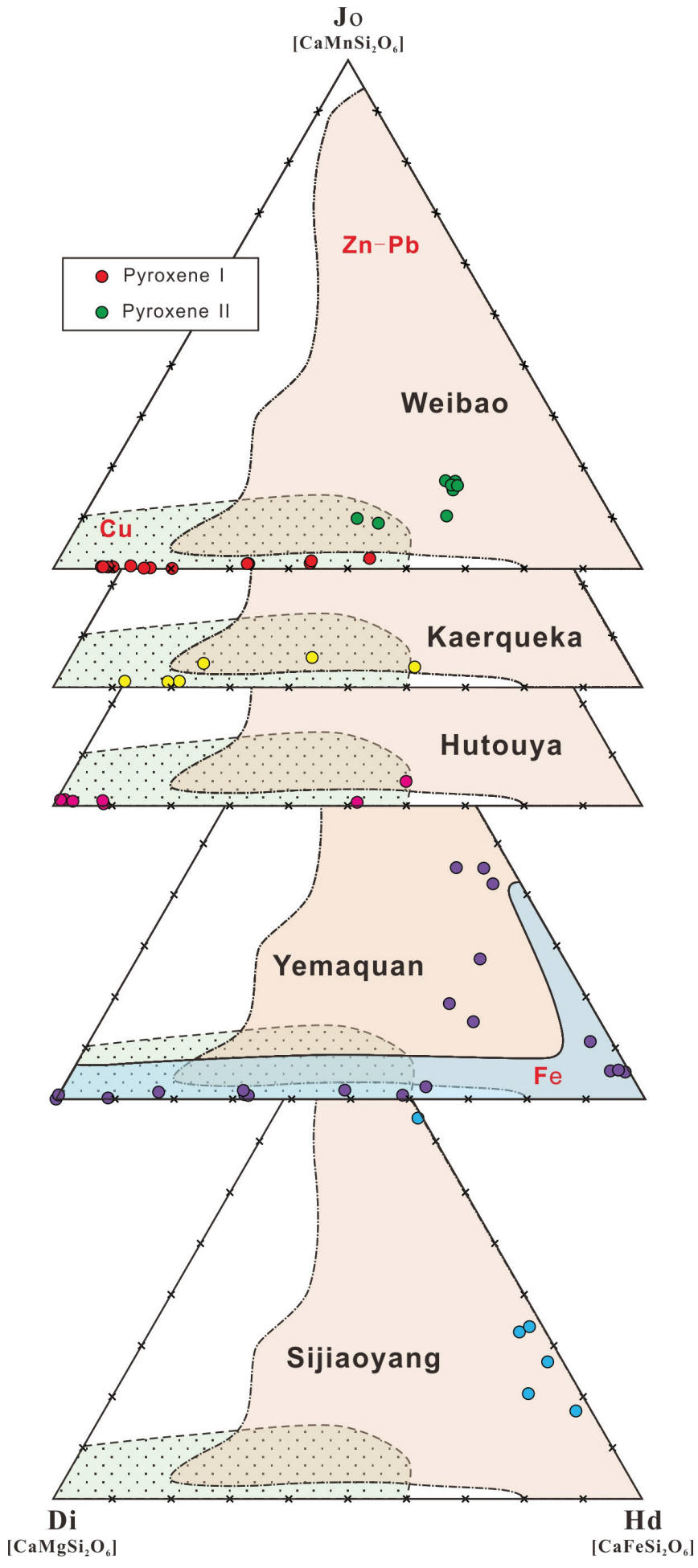
Jo
[CaMnSi2O6]
Pyroxene I
Pyroxene II
Zn–Pb
Weibao
Cu
Kaerqueka
Hutouya
Yemaquan
Fe
Sijiaoyang
Di
[CaMgSi2O6]
Hd
[CaFeSi2O6]

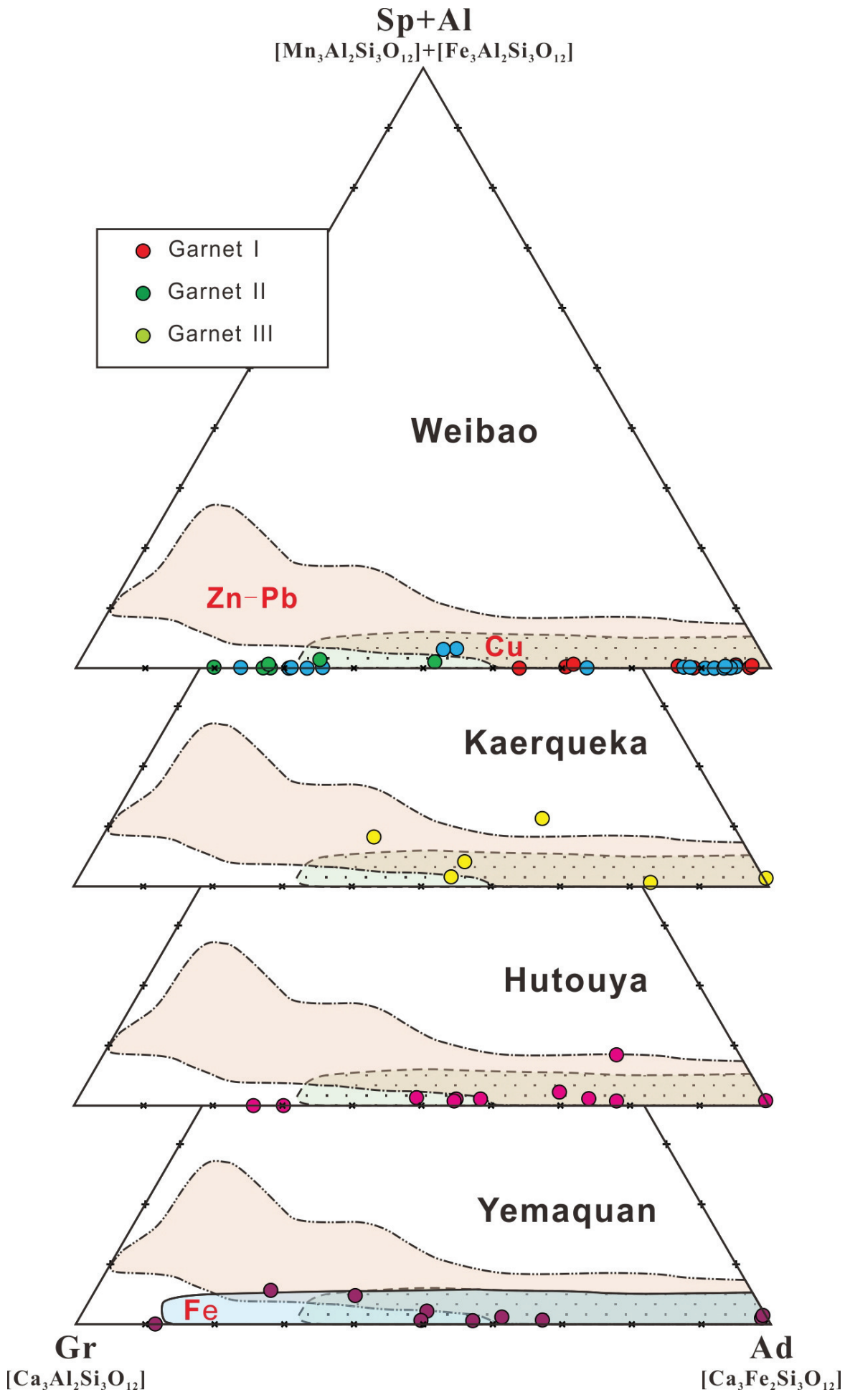
Sp+Al
[Mn3Al2Si3O12]+[Fe3Al2Si3O12]
Garnet I
Garnet II
Garnet III
Weibao
Zn-Pb
Cu
Kaerqueka
Hutouya
Yemaquan
Fe
Gr
[Ca3Al2Si3O12]
Ad
[Ca3Fe2Si3O12]

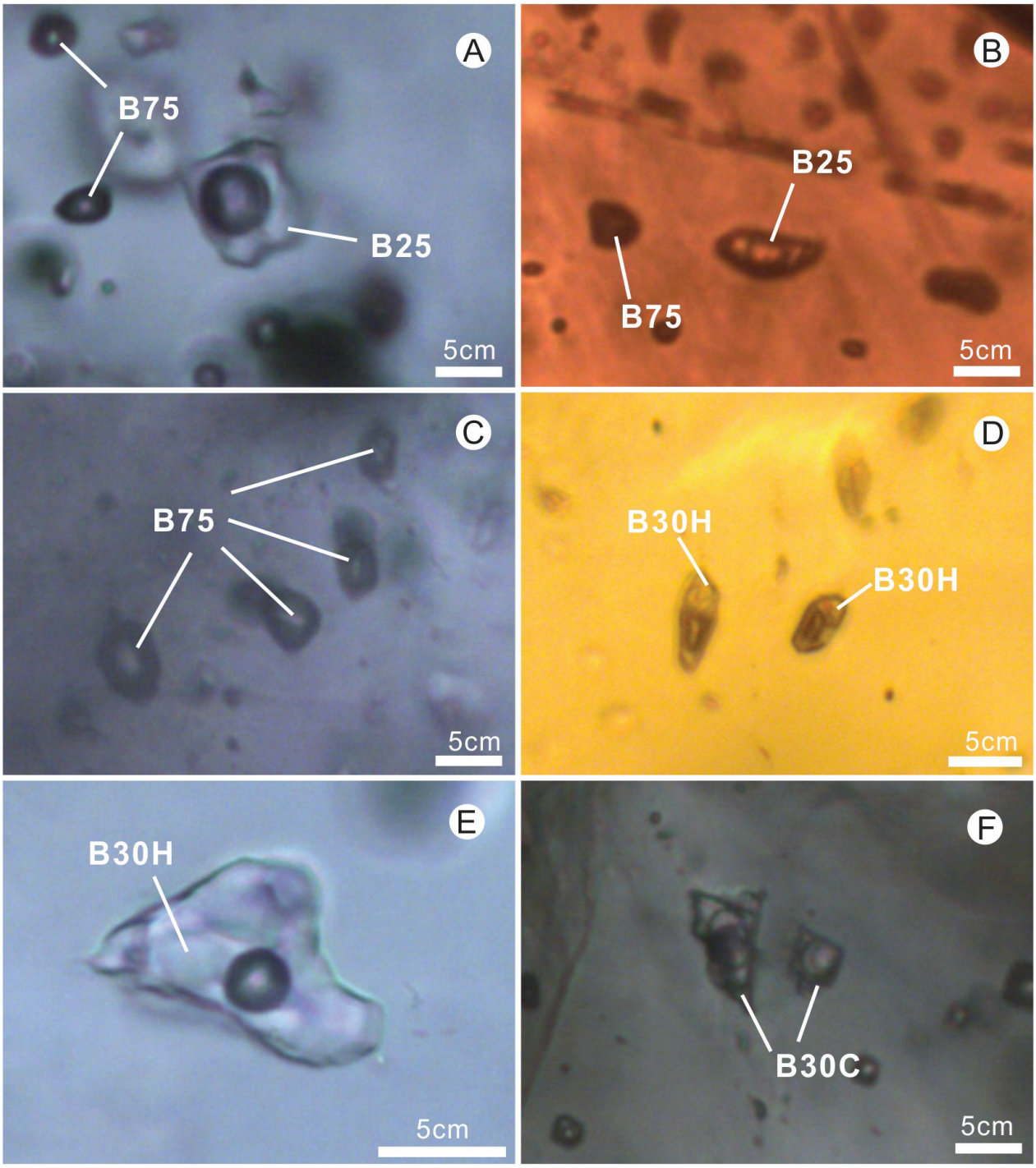
A
B75
B25
5cm
B
B25
B75
5cm
C
B75
5cm
D
B30H
B30H
5cm
E
B30H
5cm
F
B30C
5cm

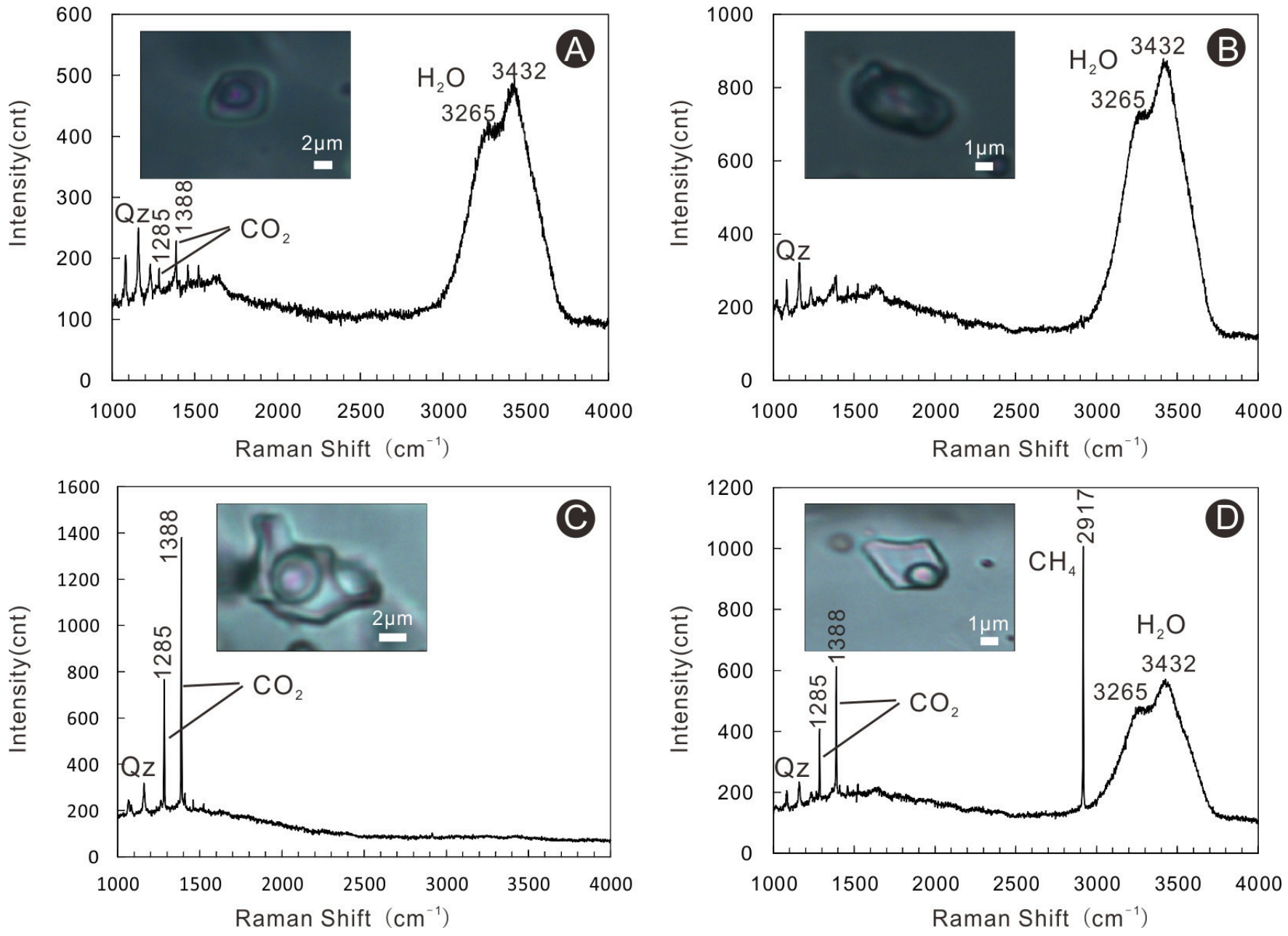
A
2μm
Qz
1285
1388
CO2
H2O
3265
3432
Intensity(cnt)
Raman Shift (cm-1)
B
1μm
Qz
H2O
3265
3432
C
2μm
1388
1285
CO2
Qz
D
1μm
1388
1285
CO2
Qz
CH4
2917
H2O
3265
3432

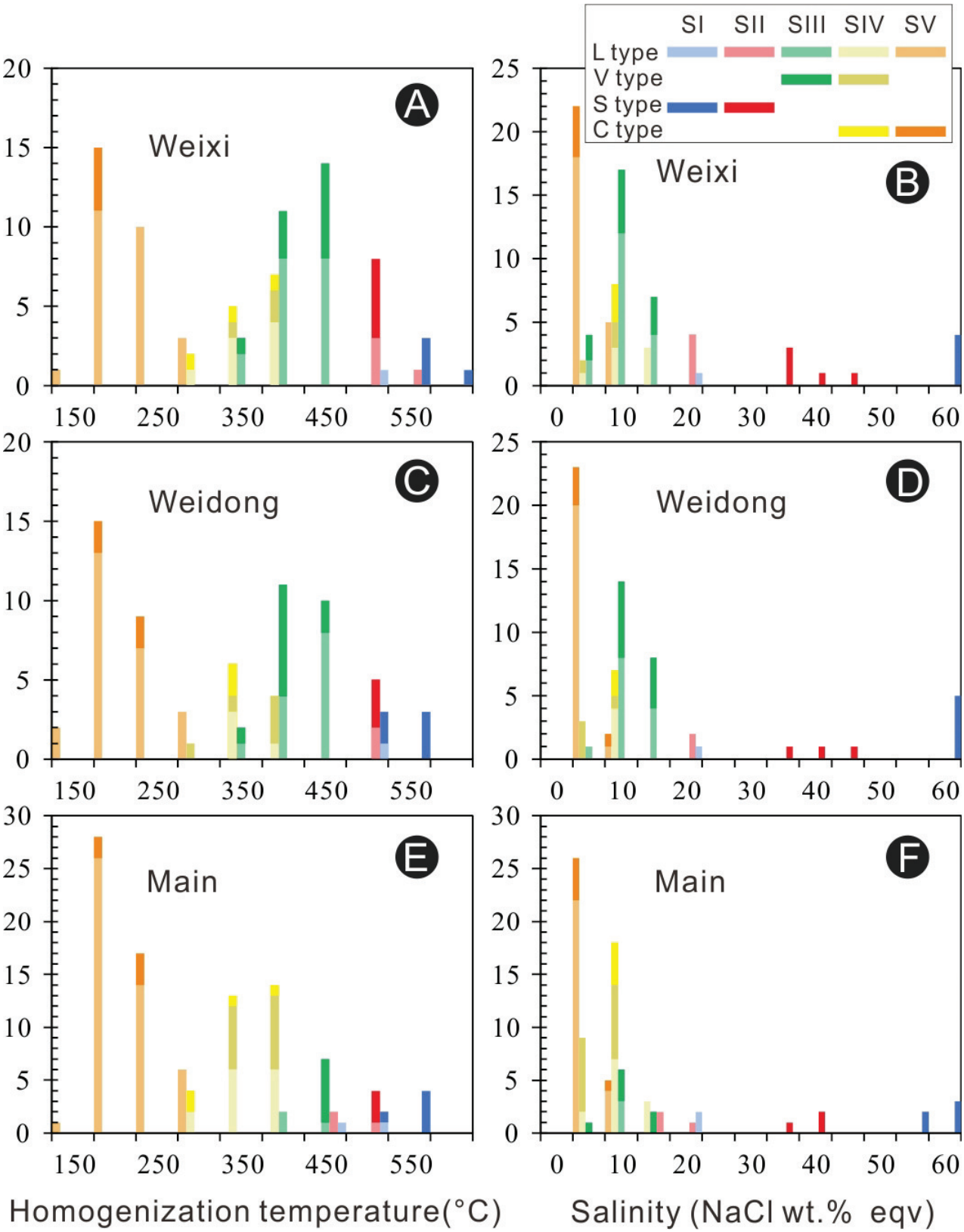
SI
SII
SIII
SIV
SV
L type
V type
S type
C type
A
Weixi
B
Weixi
C
Weidong
D
Weidong
E
Main
F
Main
Homogenization temperature(°C)
Salinity (NaCl wt.% eqv)

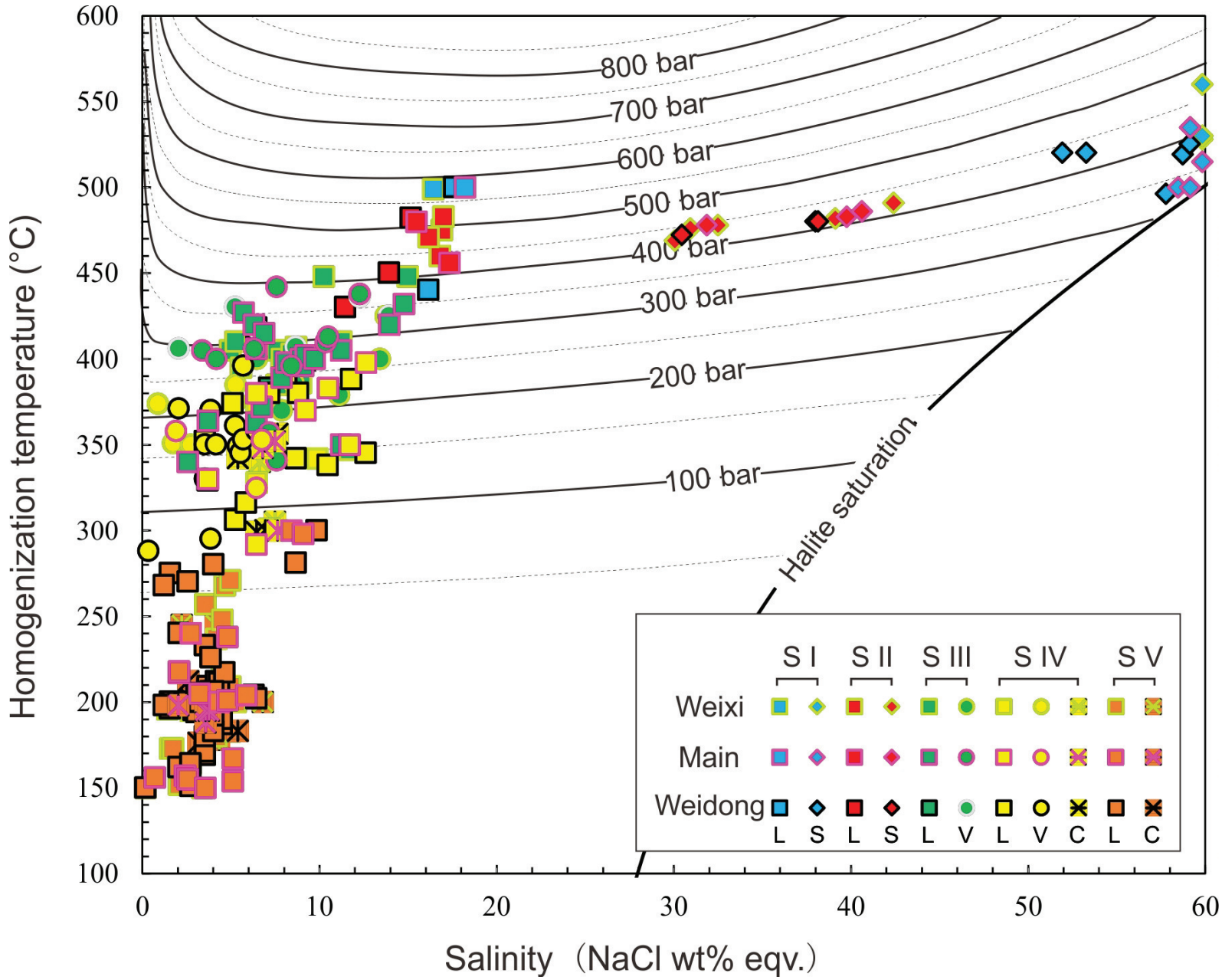
Homogenization temperature (°C)
Salinity （NaCl wt% eqv.）
800 bar
700 bar
600 bar
500 bar
400 bar
300 bar
200 bar
100 bar
Halite saturation
S I
S II
S III
S IV
S V
Weixi
Main
Weidong
L S L S L V L V C L C

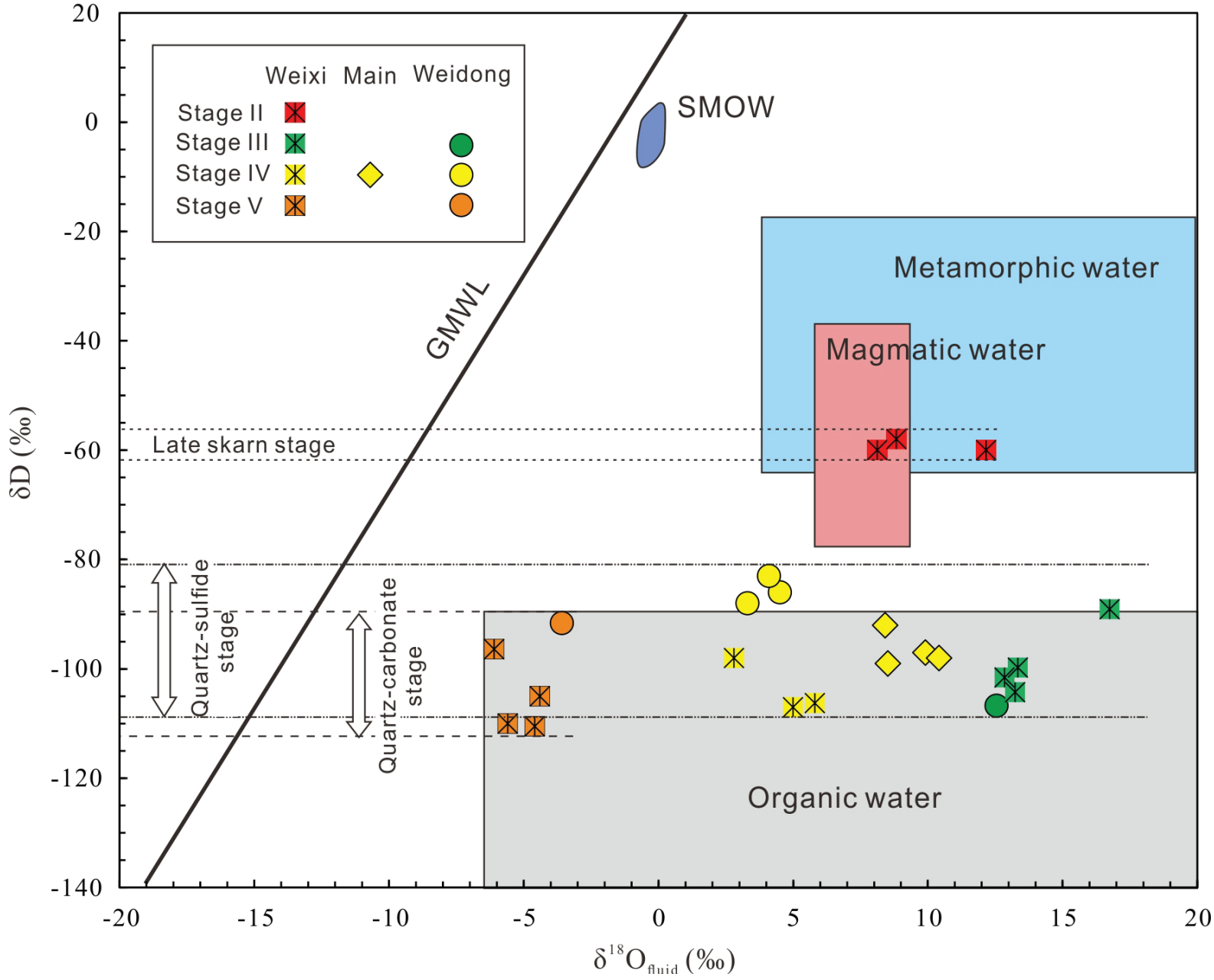
Weixi Main Weidong
Stage II
Stage III
Stage IV
Stage V
SMOW
GMWL
Metamorphic water
Magmatic water
Late skarn stage
Quartz-sulfide stage
Quartz-carbonate stage
Organic water
δD (‰)
δ18Ofluid (‰)
20
0
-20
-40
-60
-80
-100
-120
-140
-20
-15
-10
-5
0
5
10
15
20

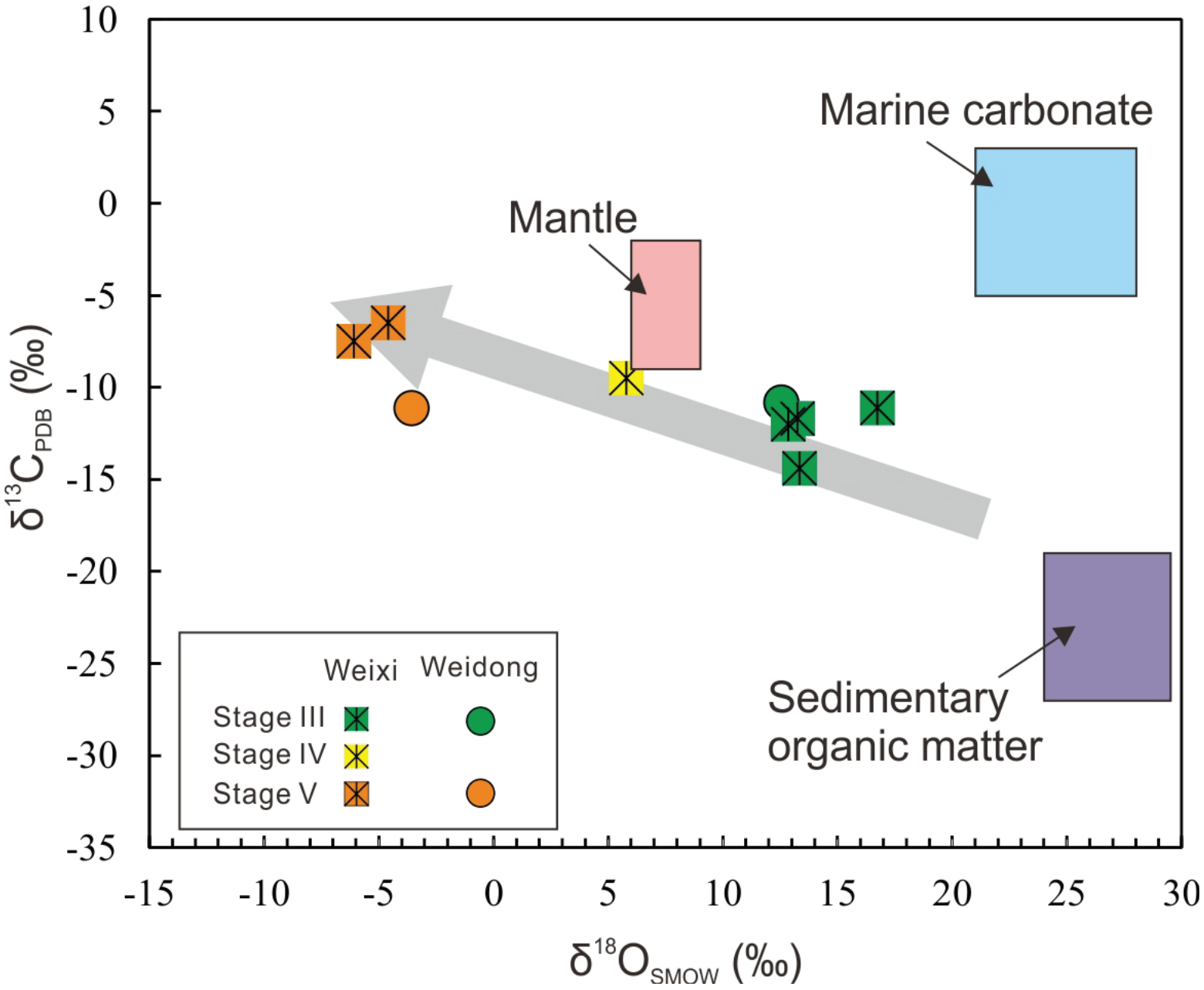
Marine carbonate
Mantle
Sedimentary
organic matter
Weixi
Weidong
Stage III
Stage IV
Stage V
δ13CPDB (‰)
δ18OSMOW (‰)
10
5
0
-5
-10
-15
-20
-25
-30
-35
-15
-10
-5
0
5
10
15
20
25
30

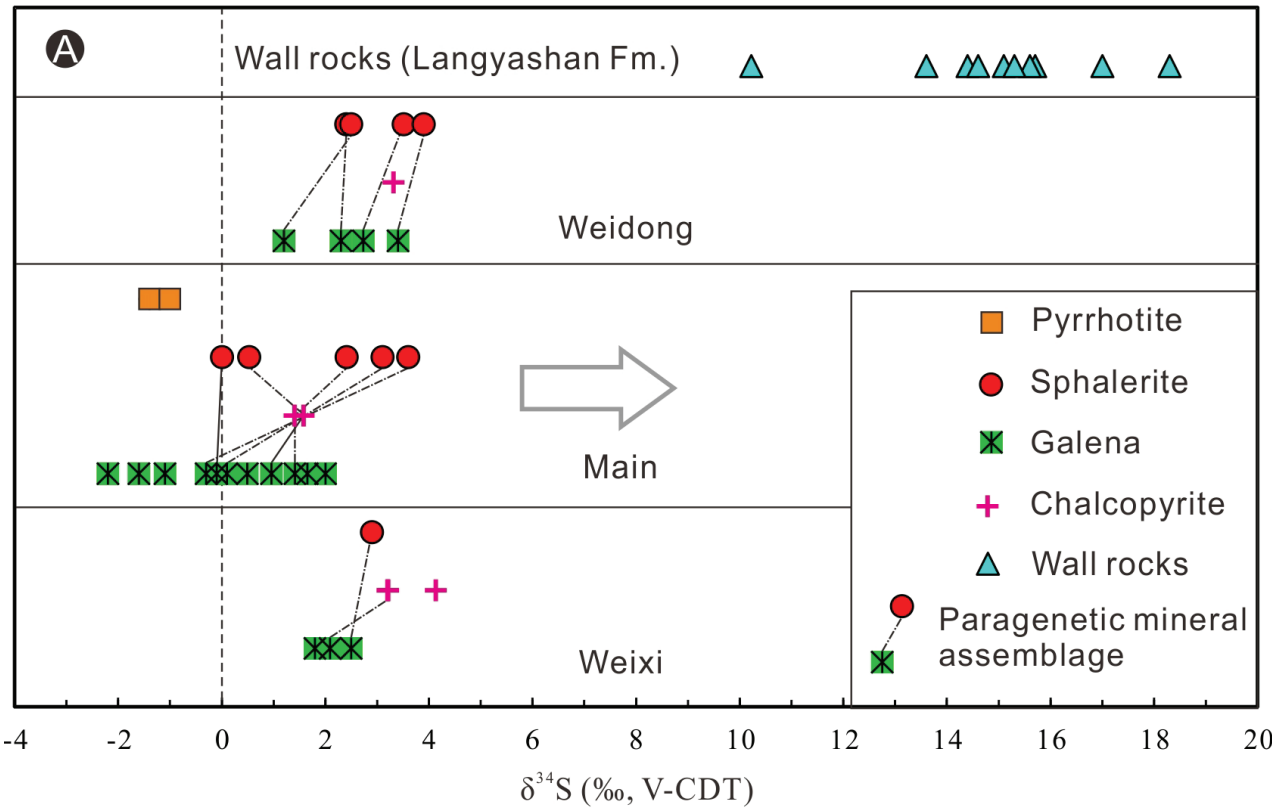
A
Wall rocks (Langyashan Fm.)
Weidong
Main
Weixi
Pyrrhotite
Sphalerite
Galena
Chalcopyrite
Wall rocks
Paragenetic mineral assemblage
-4
-2
0
2
4
6
8
10
12
14
16
18
20
δ34S (‰, V-CDT)

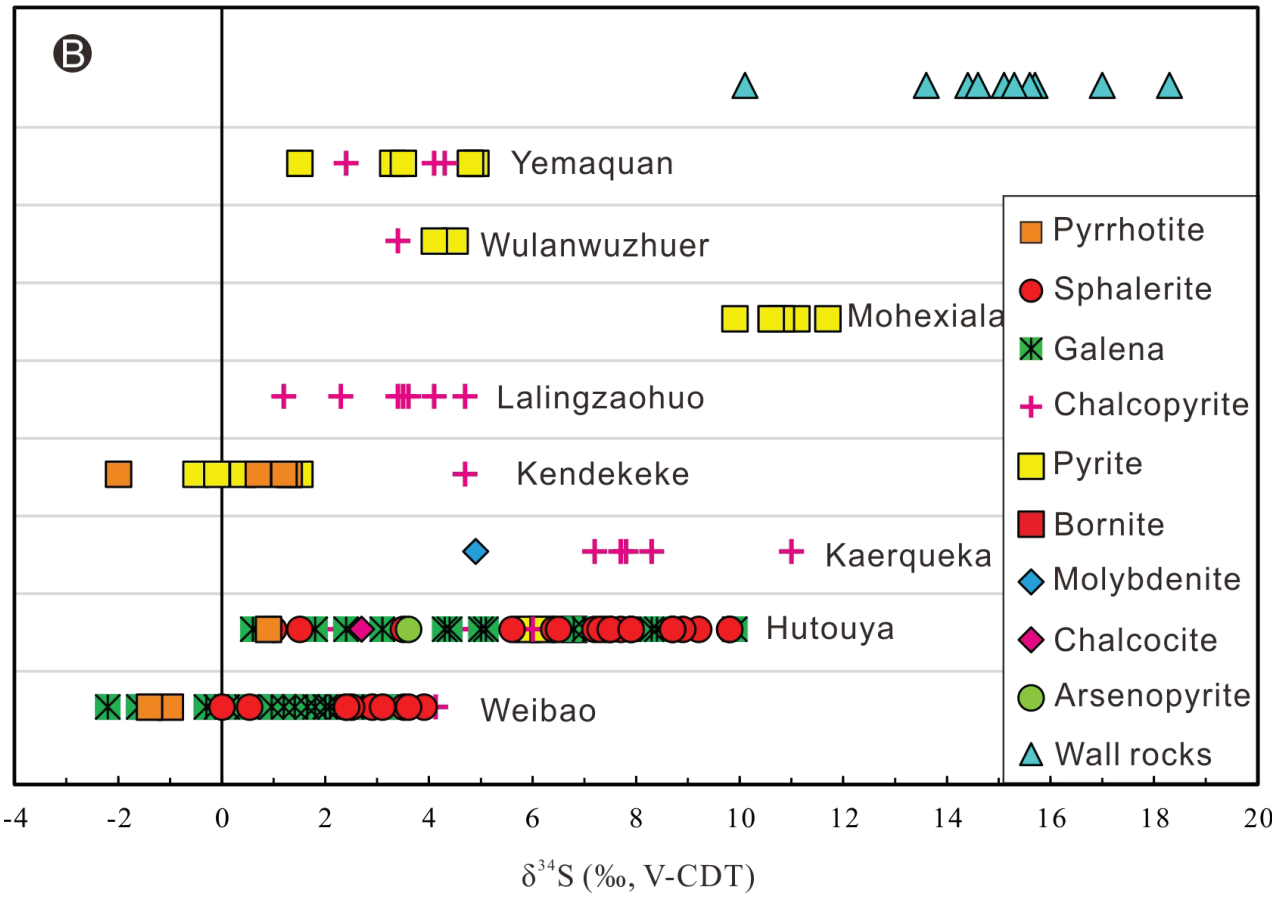
B
Yemaquan
Wulanwuzhuer
Mohexiala
Lalingzaohuo
Kendekeke
Kaerqueka
Hutouya
Weibao
Pyrrhotite
Sphalerite
Galena
Chalcopyrite
Pyrite
Bornite
Molybdenite
Chalcocite
Arsenopyrite
Wall rocks
-4
-2
0
2
4
6
8
10
12
14
16
18
20
δ34S (‰, V-CDT)

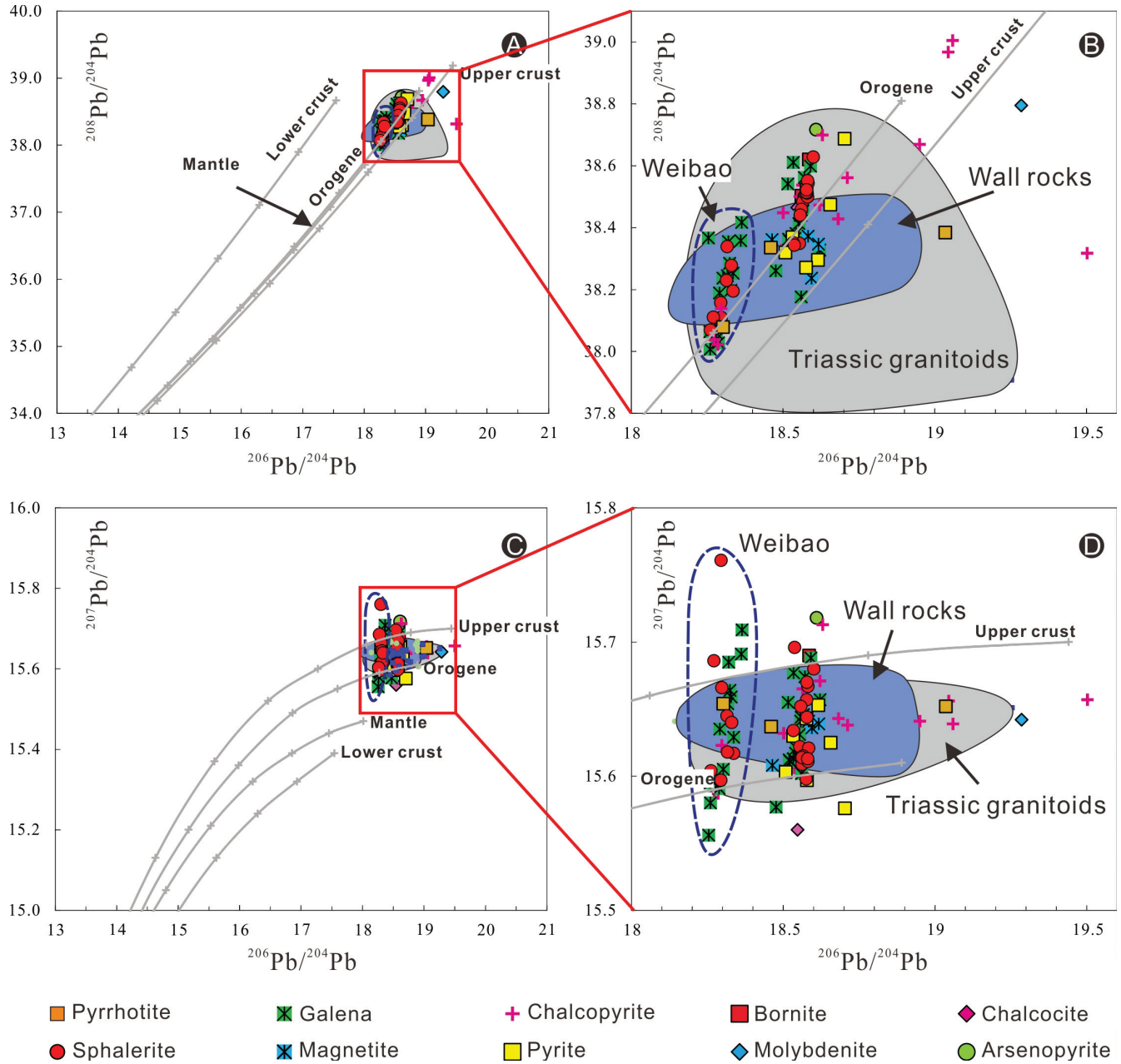
A
B
C
D
Mantle
Lower crust
Orogene
Upper crust
Weibao
Wall rocks
Triassic granitoids
$^{208}Pb/^{204}Pb$
$^{207}Pb/^{204}Pb$
$^{206}Pb/^{204}Pb$
Pyrrhotite
Galena
Chalcopyrite
Bornite
Chalcocite
Sphalerite
Magnetite
Pyrite
Molybdenite
Arsenopyrite

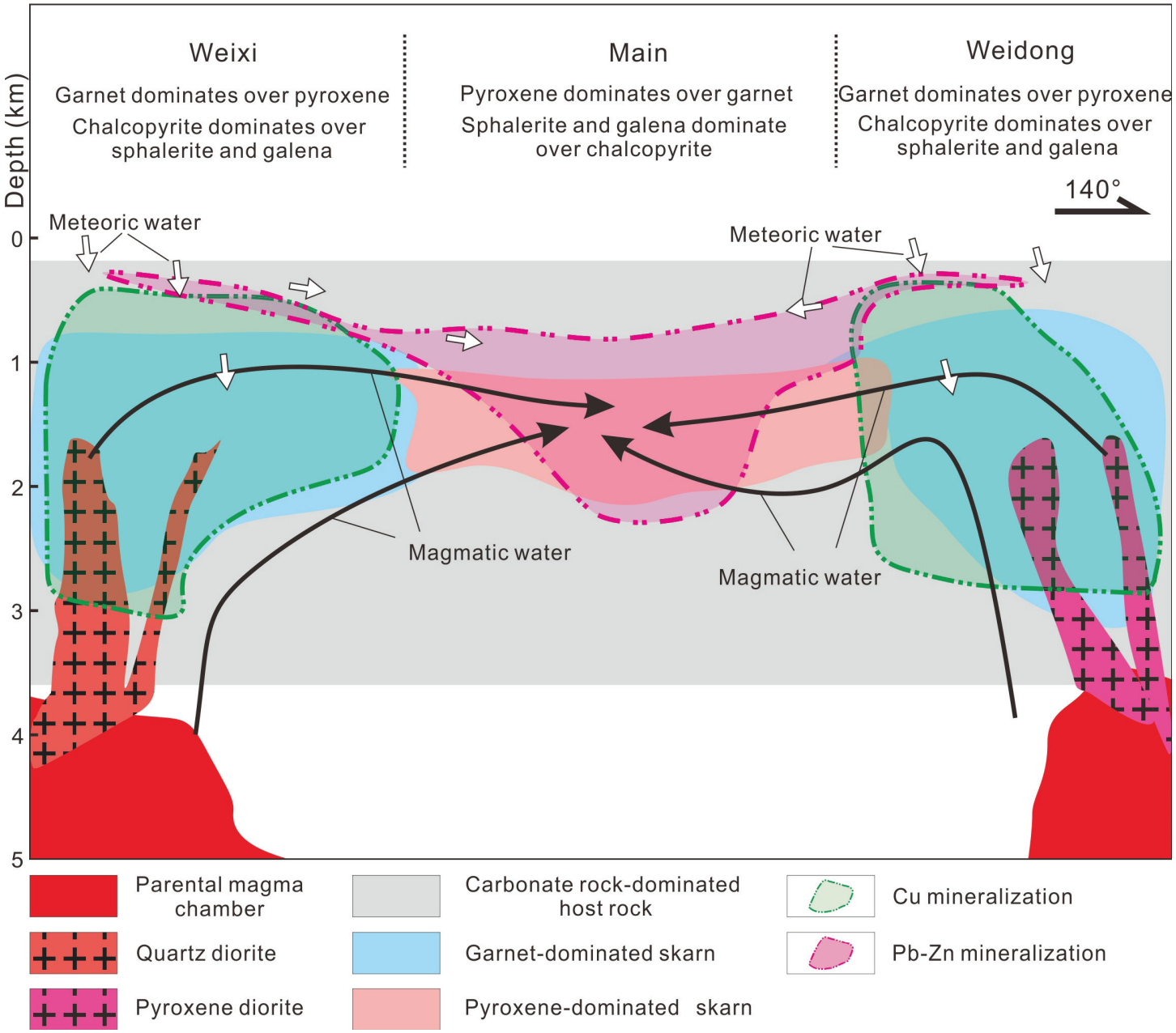
Weixi
Garnet dominates over pyroxene
Chalcopyrite dominates over sphalerite and galena
Main
Pyroxene dominates over garnet
Sphalerite and galena dominate over chalcopyrite
Weidong
Garnet dominates over pyroxene
Chalcopyrite dominates over sphalerite and galena
140°
Depth (km)
0
1
2
3
4
5
Meteoric water
Meteoric water
Magmatic water
Magmatic water
Parental magma chamber
Quartz diorite
Pyroxene diorite
Carbonate rock-dominated host rock
Garnet-dominated skarn
Pyroxene-dominated skarn
Cu mineralization
Pb-Zn mineralization